Development of a Beamline System for Characterization of X-ray and Neutron Optics

by

Andrew O. Ames

Submitted to the Department of Physics
in partial fulfillment of the requirements for the degree of

Bachelor of Science in Physics

at the

MASSACHUSETTS INSTITUTE OF TECHNOLOGY

June 2016

Author ..... Signature redacted .....
Department of Physics
May 6, 2016

Certified by.. Signature redacted .....
Suzanne Romaine
Physicist, Harvard-Smithsonian Center for Astrophysics
Thesis Supervisor

Certified by..... Signature redacted .....
Marshall Bautz
Senior Research Scientist, MIT Department of Physics
Thesis Supervisor

Accepted by.. Signature redacted .....
Nergis Mavalvala
Senior Thesis Coordinator, MIT Department of Physics

Development of a Beamline System for Characterization of X-ray and Neutron Optics

by

Andrew O. Ames

Submitted to the Department of Physics
on May 6, 2016, in partial fulfillment of the
requirements for the degree of
Bachelor of Science in Physics

Abstract

In this thesis, I present a beamline system designed and built at the Harvard-Smithsonian Center for Astrophysics (CfA) to measure the reflectivity and resolution of small diameter multilayer coated Wolter optics. These optics, used for imaging of x-rays and neutrons, have numerous applications in areas such as medicine, fusion research and planetary science. The beamline consists of a divergent x-ray source, an energy sensitive detector, and a set of precise, computer controlled motorized stages for alignment. A dedicated software package was developed to interface with the detector and stages using the Python programming language. The beamline was used to measure the reflectivity and spatial resolution of two x-ray optics recently fabricated at the CfA. These results are presented and compared with theoretical models for reflectivity from a multilayer surface.

Thesis Supervisor: Suzanne Romaine
Title: Physicist, Harvard-Smithsonian Center for Astrophysics

Thesis Supervisor: Marshall Bautz
Title: Senior Research Scientist, MIT Department of Physics

Acknowledgments

I would first like to thank my thesis advisor, Suzanne Romaine. I'll forever be grateful for the chance she took in hiring me two years ago, and for all the opportunities she's given me since then. I've learned so much from her throughout my work at the CfA and especially in writing this thesis. More than that, though, working in Suzanne's lab has reignited my love of science. Before I started working at the CfA, I was on leave from MIT and unsure whether I would ever return to physics. Now, I have no doubt that this is what I want to do.

I want to also thank Ric Bruni, who has been there consistently to offer encouragement and help, and who always made coming to the lab fun. Kiran Kilaru provided so much of the knowledge and guidance that made building this beamline possible, and I truly appreciate her patient assistance. I also would like to thank my academic advisor, Bob Jaffe, for his help throughout my career at MIT and for continuing to believe that I could succeed even when I wasn't at my best. And thanks to Mark Bautz, for taking the time to support this thesis and provide advice along the way.

I would not have made it through this last year at MIT without the love and support of my family, my friends, and my wonderful housemates. You all kept me sane and grounded throughout my most difficult times and I couldn't have asked for a better group of people by my side.

And especially, Erin Tomlinson. Your success has been an inspiration to me, and your encouragement has kept me striving to achieve more than I thought possible. I can't thank you enough for being my friend throughout all these crazy years.

Contents

1 Introduction and motivation **13**

1.1 History of x-ray optics 14

1.2 Recent developments 15

1.3 New applications 16

1.3.1 Filter for high-energy experiments 17

1.3.2 Neutron imaging 17

1.3.3 X-ray optics for planetary missions 18

1.3.4 Small animal radionuclide imaging 18

2 Multilayer coated x-ray optics **19**

2.1 Total external reflection of x-rays 19

2.2 Wolter geometry 20

2.3 Multilayer reflectance 23

2.3.1 Fresnel reflection and transmission 25

2.3.2 Névot-Croce factor 26

2.3.3 Recursive calculation of reflection from a multilayer film . . . 28

2.4 Optic fabrication 29

2.4.1 Sputtering of multilayer films 30

2.4.2 Nickel-cobalt electroforming 31

3 Beamline apparatus **33**

3.1 X-ray sources 35

3.2 CdTe detector 37

3.2.1 Theory of operation 37
3.2.2 Energy calibration 39
3.3 Optic and detector mounts 41
3.4 Control software 43
3.5 Alignment procedure 44
3.5.1 Initial visual alignment 44
3.5.2 Alignment with x-ray source 45

4 Measurement procedures and results **49**
4.1 Measurement procedures 49
4.1.1 Reflectivity 49
4.1.2 Resolution 50
4.2 Results 51
4.2.1 Optic R3 52
4.2.2 Optic R6 55

5 Conclusions **61**

A Low energy x-ray measurement **65**

List of Figures

1-1 Illustration of a Wolter optic from Wolter's U.S. patent 14

1-2 Illustration of the mirrors of Chandra X-ray Observatory 15

1-3 Photograph of the XMM-Newton mirror assembly 16

2-1 Total external reflection of x-rays 20

2-2 Wolter Type I geometry 21

2-3 Collecting area of a Wolter optic 22

2-4 Critical angle of nickel for various photon energies 24

2-5 Diagram of Bragg reflection from a multilayer film 25

2-6 Reflection and transmission of a plane wave at an interface 25

2-7 Comparision of reflectivity with and without a multilayer coating . . 29

3-1 Photograph of the beamline with details of main components 34

3-2 W tube emission spectra for various applied voltages 35

3-3 X-ray transmission in air 37

3-4 CdTe detector diode geometry 38

3-5 CdTe detector calibration spectra 41

3-6 Optic coordinate system 42

3-7 Photograph of an optic with stainless steel mounting structure 42

3-8 Visible light alignment of the optic 45

3-9 Plot of the optic pitch alignment scan 46

3-10 Software display during the final detector alignment 47

4-1 Optic R3 raw data and background spectrum 53

4-2 Optic R3 calculated reflectivity and IMD model 53
4-3 Power spectrum fit for optic R3 55
4-4 Optic R6 raw data and background spectrum 56
4-5 Optic R6 calculated reflectivity and IMD model 57
4-6 Power spectrum fit for optic R6 59

A-1 X-ray transmission in air and in helium 65
A-2 Silicon drift detector geometry 66
A-3 SDD calibration spectra 67

List of Tables

3.1 Characteristic lines of various x-ray tube target materials 36

3.2 Spectral lines used in CdTe detector calibration 40

4.1 Deposition thickness parameters of the R3 SiW multilayer film 52

4.2 IMD parameters for models of optic R3 54

4.3 Model thickness parameters of the R3 SiW multilayer film with increased d-spacing 55

4.4 Deposition thickness parameters for R6 SiW multilayer film 56

4.5 IMD parameters for models of optic R6 57

4.6 Depth-graded model parameters for R6 SiW multilayer film. 58

A.1 Spectral lines used in silicon drift detector calibration 67

Chapter 1

Introduction and motivation

As the Chandra and XMM-Newton X-ray Observatories continue to return valuable astrophysical data more than 15 years after their launches, the development of new technologies is underway for the next generation of x-ray telescopes. At the Harvard-Smithsonian Center for Astrophysics (CfA), we are developing techniques to fabricate optics that will probe higher energy bands, while being thinner and lighter to meet the strict mass budgets of future space-based x-ray observatories.

To aid in the research and development of these new techniques, we have built a dedicated x-ray beamline that will allow in-house measurement of the optics fabricated at CfA. This in-house testing will reduce the time needed to evaluate prototype optics, allowing us to considerably shorten our development time.

The bulk of my work in this thesis has been designing and building the x-ray testing beamline and developing the software to control its various parts, enabling fast and accurate alignment, measurement, and data analysis. This work was motivated by a number of recent developments in x-ray focusing technology and innovative applications of these techniques, which are discussed in the remainder of this introduction. Chapter 2 discusses the theoretical basis for x-ray optics and a summary of the optic fabrication process employed at CfA. In Chapters 3 and 4 I present the main focus of my thesis—the physical details of the beamline and the results of measurements performed on two optics recently fabricated at CfA. Chapter 5 concludes with a discussion of future work, including improvements to the beamline and its software.

1.1 History of x-ray optics

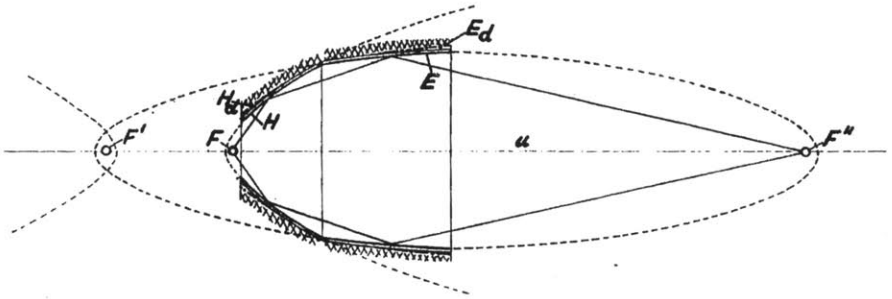

Figure 1-1: Illustration of a Wolter optic from Wolter's U.S. patent [32]. E designates the ellipsoid portion of the system, and H the hyperboloid. F and F'' are the two focal points of the optic.

In 1952, Hans Wolter proposed a design for focusing x-rays using reflection at small (grazing) angles from a set of two mirrors, which are surfaces of revolution (a hyperboloid and an ellipsoid) about the optical axis [32, 33]. An illustration of his design can be seen in Fig. 1-1. This new geometry that he proposed overcame issues of spherical aberration that had plagued earlier methods for x-ray focusing. Although his design was primarily intended for use in x-ray microscopy, the astronomical community recognized that it could be applied to develop optics for use in x-ray telescopes. These optics would provide imaging capabilities to replace the Geiger counters that were previously used to detect x-rays in space. The first astrophysical x-ray telescope, launched by NASA in 1978, was the Einstein Observatory [9].

In 1999, two groundbreaking x-ray observatories were placed into orbit and continue to return astronomical data today. The Chandra X-ray Observatory [30], launched by NASA in July of that year, employed four nested sets of highly polished iridium-coated glass mirrors. A schematic of these optics is shown in Fig. 1-2. Chandra is capable of imaging x-rays with energies between 0.1 and 10 keV, and has an unsurpassed angular resolution of 0.5 arc seconds.

In December 1999, the European Space Agency (ESA) launched the XMM-Newton observatory [17]. XMM-Newton also operates in the 0.1-10 keV energy band, and has a 15 arc second resolution. XMM-Newton is unique in that it employs 58 thin

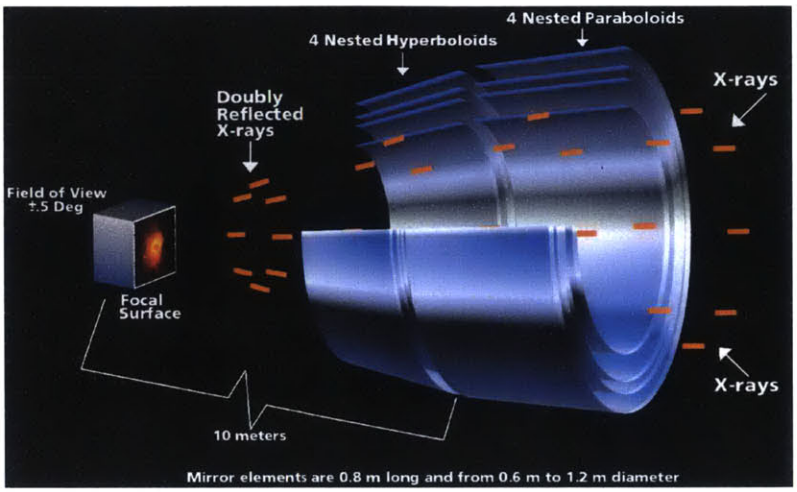

Figure 1-2: An illustration of the mirror system in use aboard the Chandra X-ray Observatory, courtesy of NASA/CXC/D.Berry.

electroformed mirrors to achieve a high collecting area, about four times that of Chandra. These mirrors are shown in Fig. 1-3.

Today, Chandra and XMM-Newton continue to observe x-ray sources and collect new data to study various high-energy processes in the universe. Programs at both ESA and NASA are actively developing the next generation of x-ray observatories, for which new technologies are currently being created at CfA and elsewhere.

1.2 Recent developments

The electroforming process used to produce the thin mirrors used in XMM-Newton has been refined by work at NASA's Marshall Space Flight Center (MSFC) [8]. The development of new alloys and the refinement of process parameters have resulted in the ability to fabricate optics with increased strength and decreased thickness compared to those used in XMM-Newton.

In order to expand the energy range of x-ray optics, new materials have been developed for the reflective mirror surfaces. Multilayer films, consisting of alternating layers of high and low density materials, are able to increase the energy passband of a mirror surface by an order of magnitude using constructive interference [16]. This type of coating was used on the mirrors for NuSTAR (Nuclear Spectroscopic

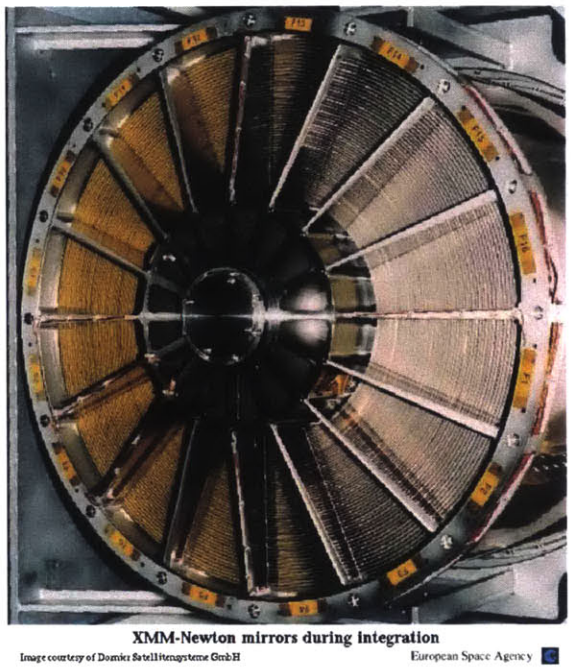

Figure 1-3: A photograph of the XMM-Newton mirror assembly, showing the 58 nested thin electroformed mirrors. Thinner mirrors allow much greater collecting area but sacrifice spatial resolution. Image courtesy of Dornier Satellitensysteme GmbH and ESA.

Telescope Array), launched in 2012, which has an energy range of 3-79 keV [12].

1.3 New applications

Over the past few years, new applications of x-ray optics have been developed at CfA in collaboration with colleagues at MSFC, MIT, and Lawrence Livermore National Laboratory (LLNL). The optics for these applications are much smaller in scale than those used in astrophysical observatories but continue to use the Wolter design. While telescope optics have diameters on the order of a meter and focal lengths of 10 meters or more, the typical diameters of these new optics are smaller by an order of magnitude or more.

For these smaller optics, it is difficult to coat the inside of a mirror shell with a multilayer film using the techniques used to coat large telescope optics. A new fabrication process has been developed at CfA to allow reliable coating of multilayer

films onto small diameter optics [27]. This new process has opened up a wide range of applications that are currently in development.

1.3.1 Filter for high-energy experiments

Multilayer films can be employed to selectively reflect narrow energy bands of x-ray photons. Therefore, they can be used to extract information from high energy density environments, such as in fusion experiments, that would otherwise be difficult to measure. Scientists at CfA and LLNL are collaborating to develop multilayer-coated Wolter optics for use as a diagnostic tool in a laser-plasma interaction experiment at the Jupiter Laser Facility at LLNL [6]. These optics could achieve an order of magnitude or more improvement in throughput and improved resolving power compared to previously used diagnostic techniques, such as transmission crystal spectrometers.

It has also been proposed that multilayer coated Wolter optics could be used to measure the gamma ray[1] emissions of plutonium and uranium in spent nuclear fuel [24]. This would provide a safe manner of measuring the amount of these isotopes remaining in the spent fuel, while filtering out the intense radiation from fission products.

1.3.2 Neutron imaging

Similar to x-rays, neutrons have a refractive index $n < 1$ for most materials, meaning that it is possible to reflect them from mirror surfaces at low graze angles. Multilayer coated waveguides are currently in use at facilities such as Oakridge National Laboratory to increase the neutron beam flux over long distances [20]. By applying these multilayer films to Wolter optics, it becomes possible to focus neutrons to provide imaging capabilities. [11]. In a collaboration between scientists at CfA, MSFC and MIT, focusing neutron optics are being developed for studies of the interactions of neutrons with various materials.

[1] In nuclear and medical applications, the terms *hard x-ray* and *gamma ray* are both often used to refer to photons with energies >10 keV, but are distinguished by their origin: gamma ray refers specifically to photons produced by nuclear processes, while x-rays are produced by atomic processes.

1.3.3 X-ray optics for planetary missions

X-ray spectroscopy is an important tool for understanding the chemical and mineralogical composition of planetary bodies such as asteroids and comet nuclei. Until recently, it was impractical to include focusing x-ray optics on *in situ* missions to these bodies due to their large size and the limited space available in these spacecraft. To work around this limitation, multilayer coated Miniature X-ray Optics (MiXO) are being developed at CfA for future missions to planetary bodies. These optics will provide new data on the formation of the target bodies and of the solar system as a whole [14].

1.3.4 Small animal radionuclide imaging

Radionuclide imaging is a technique used in biological *in vivo* studies whereby a radioactive isotope is used as a marker inside an organism. Detection of the gamma rays emitted by the nuclide allow measurement of the activity of various cells and tissues in the body.

Research and testing on small animal models of human conditions and diseases, especially mouse models, is an essential aspect of many areas of biomedical research, including neuroscience, pharmacology, cancer research, and cardiology. Current research interests in small animals using radionuclide imaging require a spatial resolution on the order of 100 μm. Commonly used imaging techniques that utilize pinhole collimation have a high tradeoff between spatial resolution and efficiency. Focusing x-ray optics with multilayer coatings can achieve an order of magnitude improvement in efficiency and spatial resolution for these medical research applications [23].

Chapter 2

Multilayer coated x-ray optics

This chapter presents the basic physics underlying the theory of multilayer-coated Wolter optics. First, the general theory of total external reflection of x-rays is discussed, followed by a summary of Wolter's optical design which takes advantage of this property of x-rays. The theory of x-ray reflection from multilayer films is examined in Sec. 2.3, including a mechanism for an exact calculation of the reflections from these films. An outline of the fabrication process for these optics is presented in Sec. 2.4.

2.1 Total external reflection of x-rays

Visible light can be manipulated and focused via refraction through transparent materials with an index of refraction greater than 1. This can be seen by inspecting Snell's law,

$$\frac{\sin(\pi/2-\theta_1)}{\sin(\pi/2-\theta_2)} = \frac{\cos\theta_1}{\cos\theta_2} = \frac{n_2}{n_1}, \tag{2.1}$$

where n_1 and n_2 are the indices of refraction in two materials, and θ_1 and θ_2 are the angles of incidence and refraction, respectively, measured from the surface of the interface between the materials. If we take material 1 to be vacuum (i.e. $n_1 = 1$), we can see that for a material with $n_2 > 1$, the light will be refracted away from the surface of the interface and toward the normal direction.

In the x-ray energy band, however, most materials have an index of refraction less than unity, making focusing via refraction at near-normal incidence impossible. The solution, then, is to manipulate x-rays using total external reflection. From Eq. 2.1, we see that there exists a critical incidence angle, given in vacuum by

$$\cos\theta_c = n_2, \tag{2.2}$$

such that $\theta_2 < 0$ for all $\theta_1 < \theta_c$. In other words, an x-ray incident at an angle smaller than the critical angle is reflected off the surface of the material instead of passing through. This is illustrated in Fig. 2-1.

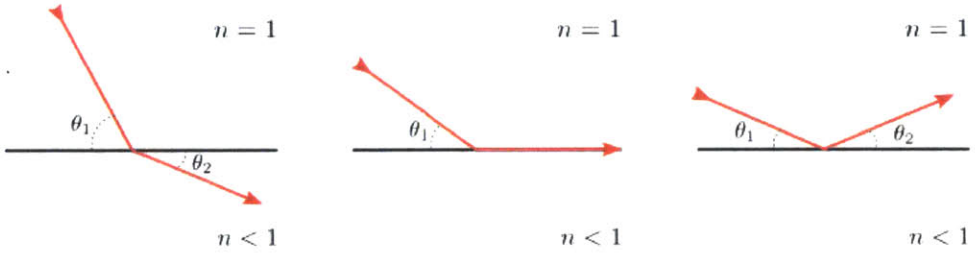

(a) $\theta_1 > \theta_c$, $\theta_2 > 0$ (b) $\theta_1 = \theta_c$, $\theta_2 = 0$ (c) $\theta_1 < \theta_c$, $\theta_2 < 0$

Figure 2-1: Illustration of total external reflection of x-rays. (a) For incident angles greater than the critical angle, the x-ray is transmitted into the material with $n < 1$. (b) If the incident angle exactly equals the critical angle, the x-ray continues to travel along the interface between the materials. (c) If the incident angle is less than the critical angle, then the x-ray is reflected from the surface back into the ambient vacuum.

2.2 Wolter geometry

Early attempts at using total external reflection to focus x-rays, such as those proposed by Kirkpatrick and Baez in 1948 [19], used parabolic mirrors which suffered from severe spherical aberration. In 1952, Hans Wolter [32, 33] proposed a system of confocal elliptical and hyperbolic mirrors that approximately fulfilled the Abbe sine condition [13], significantly reducing aberration. Wolter designed three types of systems with differing mirror geometries, but his Type I, illustrated in Fig. 2-2, is the

most commonly used in astrophysical applications and is the type used in the optics investigated in this thesis.

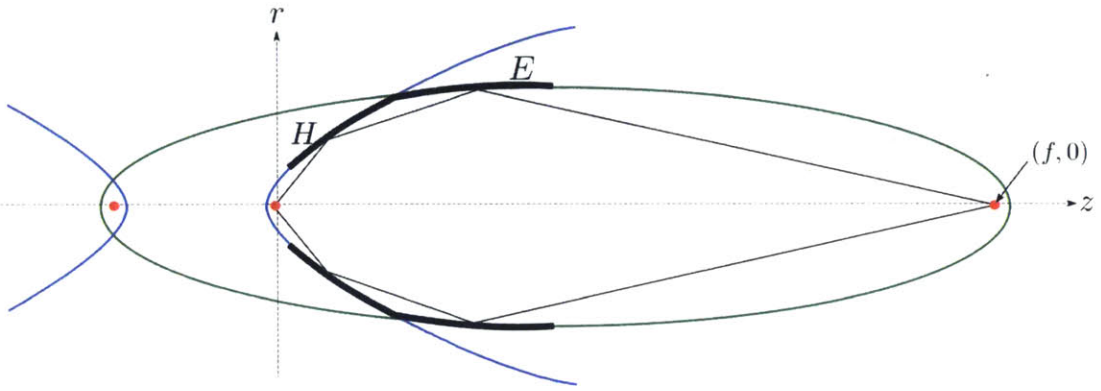

Figure 2-2: Illustration of Wolter Type I geometry. The surface of the optic, shown by a thick black line, is made up of segments of an ellipsoid (E) and a hyperboloid (H), joined at their intersection. The equations governing these surfaces are Eq. 2.3 and Eq. 2.4, respectively. The hyperboloid and ellipsoid share a common focus, indicated by the leftmost red dot. The other two red dots are the focal points of the optic. The thinner black line shows the path of a doubly reflected x-ray. In the configuration used for the beamline, the source is located at the origin and the detector at the rightward focus with coordinates $(f, 0)$, where f is given by Eq. 2.7.

In a Wolter optic, the x-rays are reflected twice from the two mirror surfaces. In the microscope orientation used for the laboratory-based optics, the rays are reflected first from the hyperboloid front mirror and then the ellipsoid mirror. The x-ray source is situated at one focus of the hyperboloid, and one focus of the ellipsoid becomes the focal point of the optic. The remaining focus of the ellipsoid is also the remaining focus of the hyperboloid.

The equations defining the ellipsoid and hyperboloid portions of the optic are

$$\frac{(z - z_{0,E})^2}{a_E^2} + \frac{r^2}{b_E^2} = 1, \tag{2.3}$$

$$\frac{(z - z_{0,H})^2}{a_H^2} - \frac{r^2}{b_H^2} = 1 \tag{2.4}$$

respectively, where z is the coordinate along the optical axis, and $r = \sqrt{x^2 + y^2}$ is the radial polar coordinate. a_E and b_E are the semi-major and semi-minor axes of the ellipsoid, and a_H and b_H are those of the hyperboloid. $z_{0,E}$ and $z_{0,H}$ denote the

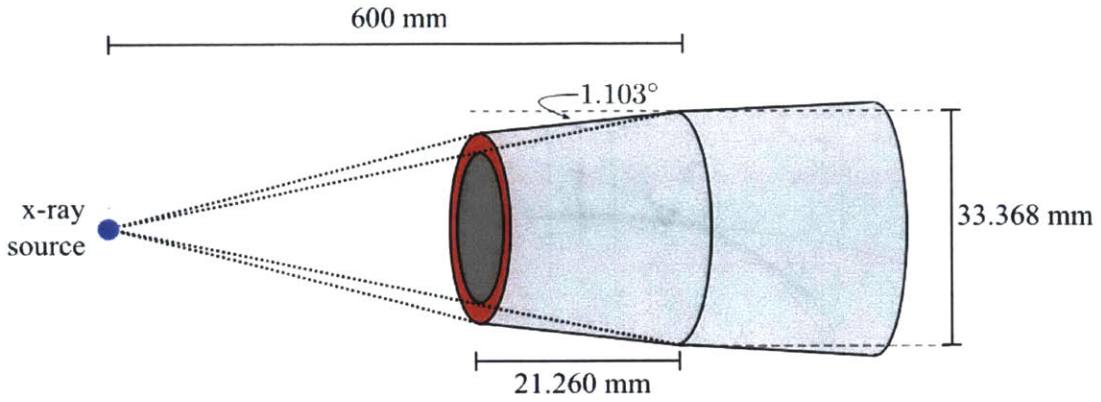

Figure 2-3: Illustration of the collecting area of the optic (not to scale). Only those rays which pass through the red ring will impinge on the hyperboloid surface of the optic. The total collecting area is given by the area of this ring, which is 18.5 mm^2 for the optics examined here.

centers of the ellipsoid and hyperboloid, respectively, and are given by

$$z_{0,E} = \sqrt{a_E^2 - b_E^2} - 2\sqrt{a_H^2 + b_H^2} \tag{2.5}$$

$$z_{0,H} = -\sqrt{a_H^2 + b_H^2} \tag{2.6}$$

In this parameterization, the x-ray source is located at the origin, and the focal point of the optic occurs at $z = f$, as shown in Fig. 2-2, where

$$f = 2\sqrt{a_E^2 - b_E^2} - 2\sqrt{a_H^2 + b_H^2}. \tag{2.7}$$

For space-based astrophysical observatories, the optic functions as a telescope, and thus the focus is at the origin of Fig. 2-2, reversed from the microscope orientation. Astrophysical x-ray sources are sufficiently distant from the optics that the incoming rays are approximately parallel. In this case, the focus f can be taken to be infinitely far away, and the ellipsoid degenerates into a paraboloid. For the optics investigated in this project, however, the sources will be at finite distance and thus the ellipsoid-hyperboloid geometry is used. These optics have a focal length of 3 m, with a source-to-optic distance of 0.6 m and optic-to-detector distance of 2.4 m, for a magnification of 4×.

Due to the requirement for small angles of incidence for total external reflection, the collecting area of Wolter I optics is relatively small compared to the surface area of the optic structure. The calculation of this collecting area is shown geometrically in Fig 2-3, using the dimensions of the optics investigated in this project. To increase the collection area, optics of various sizes with coincident focal points can be nested in a single system.

2.3 Multilayer reflectance

For photons in the x-ray regime, with energies above about 30 eV, the index of refraction n is related to the scattering factors of the atoms in the material by

$$n = 1 - \delta - i\beta = 1 - \frac{r_e}{2\pi}\lambda^2 \sum_i \rho_i f_i, \tag{2.8}$$

where r_e is the classical electron radius, λ is the photon wavelength, ρ_i is the number density of atoms of type i, and $f_i = f_1 + if_2$ is the complex atomic scattering factor of type i [29]. δ is known as the refractive index decrement, and in the high-energy limit, the real part of the atomic scattering factor f_1 is independent of λ, so $\delta \propto \lambda^2$. β is a measure of the absorption of the x-rays in matter.

For most materials, $\delta \ll 1$, so that θ_c is small. Taylor expanding Eq. 2.2 to second order in θ_c and rearranging, we find an approximate formula for the critical angle of any material,

$$\theta_c \approx \sqrt{2\delta}. \tag{2.9}$$

From Eq. 2.8, we see that δ is inversely proportional to the square of the photon energy $E = hc/\lambda$. Thus as photon energy increases, smaller and smaller incidence angles are needed to produce total external reflection, as shown in Fig. 2-4 for a nickel surface. These small angles can be achieved either by decreasing the radius of the optic, which decreases the collecting area, or by increasing the focal length, which is often impractical at high energies due to space limitations in the spacecraft used for astrophysical applications.

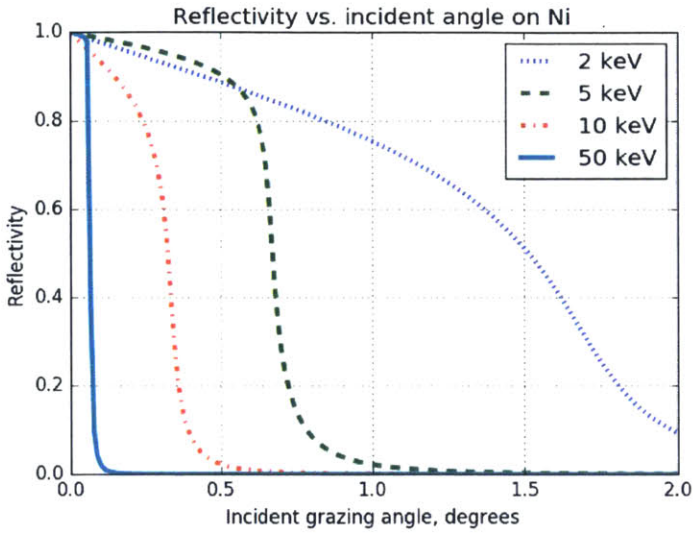

Figure 2-4: This plot shows how the critical angle of nickel decreases as the energy of the incident photons increase. The optics measured on this beamline have grazing angles of about 0.5°.

The solution, then, is to increase the reflectivity of the optical surface using constructive interference. This is accomplished by coating the reflective surface of an optic with multilayers, consisting of alternating layers of high- and low-Z materials. The thickness of the layers is tuned so that the reflections from each interface add constructively to increase the reflectivity of the surface as a whole in a certain band of energies. This effect is approximated by Bragg's law,

$$n\lambda = 2d\sin\theta, \tag{2.10}$$

where d is the layer thickness and θ is the angle of incidence. This law is valid for all positive integers n, but for these optics we will focus on the first order reflection, $n = 1$. For a given value of θ, determined by the geometry of the Wolter optic, d can be selected to choose the reflected energy band. A schematic of multilayer reflection is illustrated in Fig. 2-5.

Bragg's law is only an approximation here, however, indicating roughly where we expect the reflectivity of the multilayer film to be maximum. The different indices of refraction of the materials will alter the incident angle θ at each layer. Furthermore,

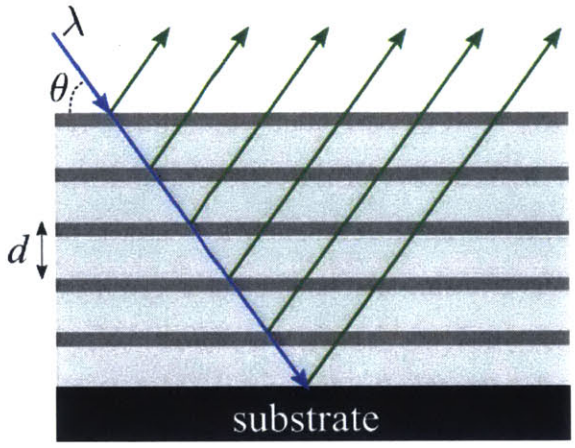

Figure 2-5: Diagram of Bragg reflection from a multilayer film by radiation with wavelength λ at incidence angle θ. The reflective metal (e.g. tungsten) is indicated by dark gray, and the lighter gray represents the spacer material (e.g. silicon).

Eq. 2.10 tells us nothing about the intensity of the reflections that we expect to measure, or how much deviation in wavelength from λ will still produce a reflection. To create a full picture the reflectance of the multilayer as a function of energy, we must calculate the coefficients of reflection and transmission.

2.3.1 Fresnel reflection and transmission

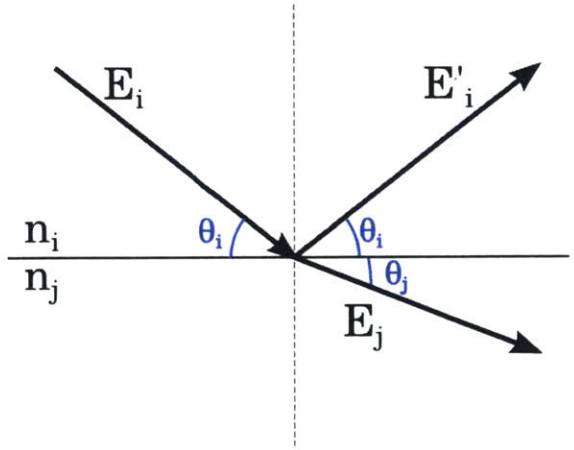

Figure 2-6: The geometry of reflection and transmission of a plane wave from an interface between two materials with different indices of refraction. A wave with amplitude E_i propagates in material i with index of refraction n_i and is incident on an interface with material j having index of refraction n_j. The wave E_i' is reflected back into material i, and E_j is transmitted into material j.

To characterize the reflectivity from a multilayer surface, we must first consider the reflection and transmission from a single boundary between two different materials. An electromagnetic wave with electric field amplitude E_i is incident on an interface between two materials with indices of refraction n_i and n_j, as shown in Fig. 2-6. If the wave is s-polarized, meaning the electric field vector is perpendicular to the plane of the interface, then the transmission coefficient is given by

$$t_{ij}^s \equiv \frac{E_j}{E_i} = \frac{2n_i \sin\theta_i}{n_i \sin\theta_i + n_j \sin\theta_j} \tag{2.11}$$

and the reflection coefficient is given by

$$r_{ij}^s \equiv \frac{E_i'}{E_i} = \frac{n_i \sin\theta_i - n_j \sin\theta_j}{n_i \sin\theta_i + n_j \sin\theta_j}. \tag{2.12}$$

For p-polarized light, with the electric field vector parallel to the plane of the interface, we have

$$t_{ij}^p \equiv \frac{E_j}{E_i} = \frac{2n_i \sin\theta_i}{n_i \sin\theta_j + n_j \sin\theta_i} \tag{2.13}$$

and

$$r_{ij}^p \equiv \frac{E_i'}{E_i} = \frac{n_i \sin\theta_j - n_j \sin\theta_i}{n_i \sin\theta_j + n_j \cos\theta_i}. \tag{2.14}$$

These relationships are known as the Fresnel equations, and a derivation can be found in [10]. The relationship between θ_i and θ_j is given by Snell's law, Eq. 2.1.

2.3.2 Névot-Croce factor

The Fresnel equations described above are valid for a perfect interface. For real films, we account for the imperfection that exists in the interface between layers using a formalism developed by Stearns [28]. We start by defining a dielectric function $\epsilon(\vec{r})$ that characterizes the dielectric constant $\epsilon = n^2$ at a point $\vec{r}$ in the interface between

material i and material j. $\epsilon(\vec{r})$ has the boundary condition that

$$\epsilon(\vec{r}) = \begin{cases} \epsilon_i, & z \to +\infty \\ \epsilon_j, & z \to -\infty \end{cases}$$

The interface profile function $p(z)$ is defined as the average value of $\epsilon(\vec{r})$ along z:

$$p(z) \equiv \frac{1}{(\epsilon_i - \epsilon_j) \iint dxdy} \iint \epsilon(\vec{r}) dxdy. \tag{2.15}$$

$p(z)$ characterizes the transition between one material and another in an interface between layers as a function of depth. In a perfect interface with no imperfections, $p(z)$ would be a step function, but in general there is some characteristic width σ, known as the microroughness, over which the interface transitions from one material to another. The cause of these imperfections during the film deposition process are discussed in Sec. 2.4.1.

We can more rigorously define σ by first defining a function $w(z) \equiv dp/dz$, which characterizes the amount of mixing between the layers at a depth z. Then σ is the variance of $w(z)$, given by

$$\sigma^2 = \int z^2 w(z) dz, \tag{2.16}$$

since $w(z)$ has zero mean by Eq. 2.15.

Stearns showed that the scattering caused by interface imperfections can be accounted for to first order by correcting the Fresnel reflection and transmission coefficients using the Fourier transform of the derivative of the interface profile, $\tilde{w}(s)$:

$$\begin{aligned} r_{ij} &= r'_{ij} \tilde{w}\left(2\sqrt{q_{z,i} q_{z,i+1}}\right), \\ t_{ij} &= t'_{ij} \end{aligned} \tag{2.17}$$

where r'_{ij} and t'_{ij} are the coefficients assuming an ideal interface, given in Sec. 2.3.1. $\tilde{w}(2\sqrt{q_{z,i} q_{z,i+1}})$ is known as the Névot-Croce factor [21], where $q_{z,i} = 2\pi \cos\theta_i / \lambda$ is the z component of the momentum transfer vector $\vec{q}$ in layer i, for radiation of wavelength λ.

The formalism described above is useful in that it is valid for any function $p(z)$ that we choose to describe the interface profile. The function used by Névot and Croce, which we have used in creating our models for this project, is the error function:

$$p(z) = \frac{1}{\sqrt{\pi}} \int_{-\infty}^{z} e^{-t^2/2\sigma^2} dt. \tag{2.18}$$

Then the resulting Névot-Croce factor is

$$\tilde{w}(2\sqrt{q_{z,i}q_{z,i+1}}) = \exp\left(-\frac{8\pi^2\sigma^2}{\lambda^2}\cos\theta_i \cos\theta_{i+1}\right). \tag{2.19}$$

2.3.3 Recursive calculation of reflection from a multilayer film

Using the Fresnel reflectivity modified by the Névot-Croce factor, we can calculate the net reflection and transmission coefficients at layer i with thickness d_i and index of refraction n_i:

$$\begin{aligned} r_i &= \frac{r_{ij} + r_j e^{2i\beta_i}}{1 + r_{ij} r_j e^{2i\beta_i}}, \\ t_i &= \frac{t_{ij} t_j e^{2i\beta_i}}{1 + r_{ij} r_j e^{2i\beta_i}}, \end{aligned} \tag{2.20}$$

where $\beta_i = 2\pi d_i n_i \cos\theta_i/\lambda$, and r_{ij} and t_{ij} are the modified Fresnel coefficients of Eq. 2.17. Then to calculate the total reflectivity of the multilayer coating, Eq. 2.20 is applied recursively, starting at the bottom layer, the substrate, and ending at the top. Because the sources used in this beamline are unpolarized, the final reflection and transmission coefficients are given by an average over the s and p polarizations. The net reflectance, which is the ratio of the energy reflected from the film to the input energy, is given by the squared amplitude of the net reflectivity of the top layer, $R = |r_{\text{top}}|^2$.

IMD [31] is a software package for modeling the reflectance of multilayer films by performing the computations described above. It includes a database of optical constants of the elements as well as many compounds, which can be used to compute the complex index of refraction for the substrate, ambient environment, and all layers

in the film, given the density and chemical composition of each component.

For a multilayer consisting of alternating bilayers, the user specifies the composition of the two layers (e.g. silicon and tungsten), the number N of bilayers, the thickness d of each bilayer, and the ratio Γ of the thickness of the top layer of the bilayer to the total thickness d. The microroughness σ is also specified for each interface in the film. IMD can then model the reflectance as a function of grazing angle or energy. We will compare IMD's predctions for our optics with the reflectivity data gathered on the beamline. An example of a model created by IMD, showing the effect of a multilayer film on reflectance, is shown in Fig. 2-7.

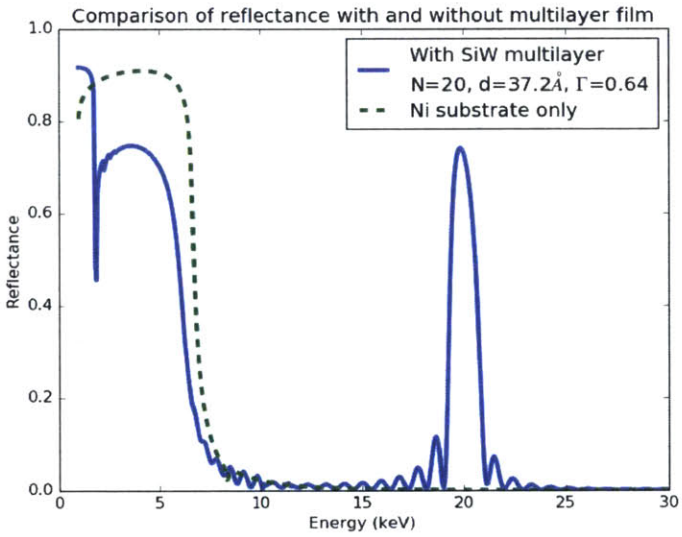

Figure 2-7: This plot shows the difference in reflectance between a pure nickel substrate and a substrate coated with a silicon-tungsten (SiW) multilayer with 20 layers of 37.2 Å thick. Both models are for an angle of incidence of 0.5°. In both plots, there is an initial plateau of reflectance which drops off for energies >8 keV. In the multilayer model, another peak in the reflectance is visible around 20 keV which falls off quickly on either side, demonstrating the bandpass capability of multilayer films.

2.4 Optic fabrication

The process of fabricating the optics measured in this thesis begins with a figured and highly polished mandrel in the desired shape of the optic. The mandrels for the

optics described here were figured and polished at MSFC. The mandrel is cleaned and passivated to create a thin oxide layer which will aid in the separation of the optic at the end of the process. The multilayer film is then deposited on the mandrel via DC magnetron sputtering, described below.

2.4.1 Sputtering of multilayer films

Sputtering occurs when a target material is bombarded with energetic particles, causing the target to eject one or more of its atoms. Inert gas ions, generally Ar^+, are used for the bombarding particles. A high voltage is applied between the target (cathode) and the substrate to accelerate the bombarding ions to sufficient energy to eject atoms from the target. The neutral ejected atoms are propelled in the direction of the substrate, coating it with the target material.

For multilayer coatings, highly uniform layer thicknesses and high densities are required to optimize the reflectivity. Additionally, the deposition process must be precise and highly repeatable to give an accurate energy response. Sputtering has an advantage over other deposition processes in that the sputtered atoms have a high kinetic energy when reaching the substrate as compared to, for example, evaporation processes. This gives the atoms more mobility in the growing film, creating a more closely-packed and uniformly thick layer.

The Wolter optic mandrels are mounted in the sputtering chamber and rotated in front of the target at a constant rate in order to evenly coat the entire surface. The deposition on the mandrel begins with a layer of carbon about 40 Å thick. This layer has a low adherence to the mandrel, which will facilitate the separation of the shell from the mandrel at the end of the fabrication process. The mandrel is then alternately sputtered with the reflective metal and the spacer material. The thickness of these layers, typically on the order of tens of angstroms, is governed by the sputtering rate, which differs by material, and the amount of time the mandrel spends exposed to the spray of atoms from the target. After all bilayers have been deposited, the film is sputtered with a top layer of platinum to provide a conductive surface for the electroforming process.

Imperfections in the interface between layers in the multilayer films can have a significant effect on the reflectivity of the optic. These imperfections can be broken down into two parameters. The roughness, σ_r, characterizes the deviation of the interface between multilayers (or the surface of the film) from its ideal shape. All films will have some amount of roughness because the packing of the atoms during the film growth is not perfect. Diffuseness (σ_D) describes the mixing at the interface of the two layer materials, usually caused by embedding of neutral Ar atoms into the film. These Ar atoms cause collisions of the atoms in the bulk of the film, causing them to move upward and mix with the higher layers. The roughness and diffuseness are related to the microroughness σ defined in Eq. 2.16 by

$$\sigma = \sqrt{\sigma_r^2 + \sigma_d^2}. \tag{2.21}$$

2.4.2 Nickel-cobalt electroforming

Electroformed Wolter optics were used in x-ray observatories such as XMM-Newton [17] because they are much thinner than the polished glass substrates used in the Chandra X-Ray Observatory [30]. A thinner substrate allows more optics to be nested, increasing the collecting area of the telescope. However, to date, electroformed optics have not yet achieved the resolution of polished glass substrates.

In contrast with the pure nickel shells used in the XMM-Newton optics, the electroplating bath at the CfA uses a NiCo alloy developed at MSFC [8]. This makes the optics less ductile for a given thickness, helping to improve their resolution by decreasing damage due to stress during the separation and handling processes.

After the mandrel has been sputtered with a multilayer film, it is mounted onto a rotating fixture and inserted into the electroplating bath. The bath is a solution containing metal ions, in this case nickel and cobalt, though which an electric field is applied, with the mandrel acting as the cathode. The anodes are two baskets containing nickel and cobalt pieces which replenish the metals as they are drawn out of the bath. The metal ions deposit onto the mandrel, on top of the multilayer film, creating a nickel-cobalt (NiCo) layer about 300 μm thick. This layer acts as a shell

which replicates the figure of the mandrel to a high precision.

After the electroplating process is complete, the aluminum mandrel is cooled in a bath of deionized water to about 0° C. The different thermal expansion coefficients of Al and Ni allow the deposit, along with the multilayer film, to separate from the mandrel. The mandrel passivation and the sputtered carbon release layer both aid in the low adherence of the shell to the mandrel, allowing separation with minimal stress on the optic. The mandrel can then be cleaned and polished for another replication.

Chapter 3

Beamline apparatus

This chapter discusses the details of the dedicated x-ray beamline that was built at CfA for the purpose of measuring small diameter x-ray optics. The beamline consists of three main physical components:

1. An x-ray source which provides a continuous spectrum of photon energies, discussed in Sec. 3.1
2. An energy-sensitive detector to measure the optic's response, discussed in Sec. 3.2
3. Precision computer-controlled motorized stages to adjust the position of the optic and detector with respect to the x-ray beam, covered in Sec. 3.3

These and other beamline components can be seen in Fig. 3-1. A custom software package was also written for this project, which controls both the detector and motorized stages. The software's functionality is briefly summarized in Sec. 3.4. The primary function of the software is to aid in the alignment process, detailed in Sec. 3.5, which is essential to accurate measurement of the optics.

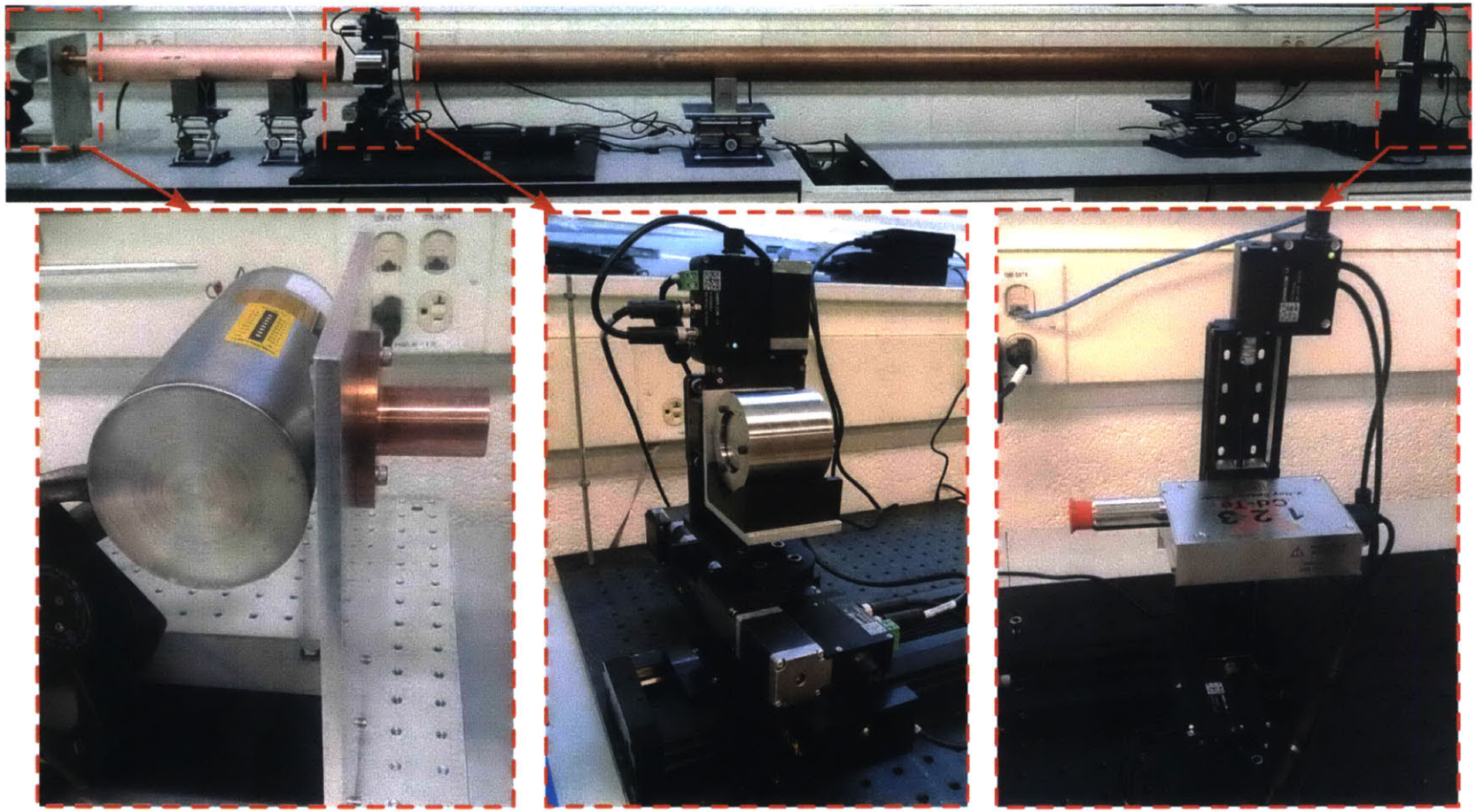

Figure 3-1: The top image is a photograph of the complete, 3 meter long beamline. The optic is mounted 0.6 m from the source. Copper tubes along the length of the beamline provide radiation shielding; additional shielding is used around the optic during operation but has been removed for the photo. On the bottom are close-up photos of the three major beamline components, from left to right: the x-ray source with copper collimator, the optic in a mounting structure on two rotary and two linear stages, and the detector on a three axis linear stage mount.

3.1 X-ray sources

The x-ray sources used in the beamline are filament-type tubes in a lead-lined stainless steel casing. The casing is filled with dielectric oil which provides both radiation shielding and heat dissipation [22]. The energy spectrum of the emitted x-rays consists of a continuous spectrum of *bremsstrahlung*, or braking radiation, and a characteristic spectrum that depends on the target material. The bremsstrahlung is emitted by the electrons ejected from the filament when they rapidly decelerate upon colliding with the target material. Thus the maximum energy of x-rays in the bremsstrahlung is $E_{\max} = eV$, where e is the electron charge and V is the tube voltage. [7]

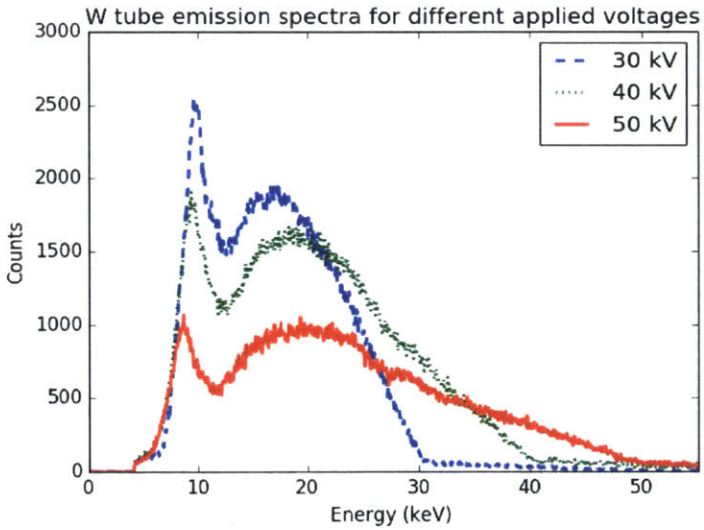

Figure 3-2: The emission spectra of a tungsten tube with three different applied voltages. The bremsstrahlung is visible as a wide hump in each spectrum, terminating at photon energy $E_{\max} = eV$. The Lα and Lβ lines of tungsten overlap into a single spike around 9.5 keV in each spectrum. All three spectra were taken at a tube current of 0.05 mA and a distance of 3 meters from the tube.

The characteristic spectrum consists of narrow maxima superimposed on the continuous spectrum, resulting from the transition of the electrons in the target to different energy levels. The full spectrum, including characteristic lines and bremsstrahlung, is shown for a tungsten tube in Fig. 3-2 at various voltages. We will be using only the bremsstrahlung, so the target material must be chosen so that there is not a characteristic line in the energy regime of interest. Tungsten, copper, and chromium tubes

were acquired for use in the beamline, and the characteristic lines of these materials are given in Table 3.1.

Table 3.1: Characteristic lines for x-ray tube target materials used in the beamline. All energies are in keV. [29]

Element	$K\alpha_1$	$K\alpha_2$	$K\beta_1$	$L\alpha_1$	$L\alpha_2$	$L\beta_1$	$L\beta_2$	$L\gamma_1$
Cr	5.415	5.496	5.947	0.573	0.573	0.583		
Cu	8.048	8.028	8.905	0.930	0.930	0.950		
W	59.318	57.982	67.244	8.398	8.335	9.672	9.962	11.286

In this beamline, the x-rays propagate 3 meters through air from the source to the detector. Attenuation of the x-rays in air means that a significant fraction of the low-energy x-rays of the spectrum are lost over this distance. As shown in Fig. 3-3, only about 10% of emitted 9 keV x-rays are transmitted the full distance to the detector, and this figure drops to less than 1% for x-rays with energies of 7.5 keV or less. This effect is visible in the spectra of Fig. 3-2 as well as the data presented in Chapter 4. It is possible to mitigate this attenuation by replacing the intermediate air with a different gas such as helium; this was not done for this thesis but the procedure is outlined in Appendix A.

A copper collimator is used in front of the x-ray tube mount to limit the size of the beam. With the collimator in place, the beam measures approximately 40 mm in diameter at the location of the optic. This is sufficient to encompass the <35 mm diameter optic while still limiting the beam size for safety reasons.

A power supply controls the voltage between the filament and the target, as well as the beam current (the flow of electrons from the filament to the target). Typically we have seen that a beam current of 0.2 mA produces an adequate flux over a reasonable collection time. The voltage is determined by the desired range of photon energies in the beam.

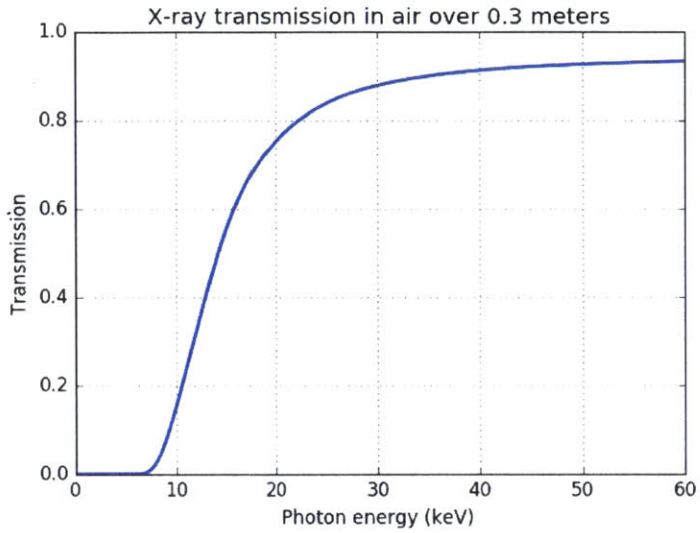

Figure 3-3: Plot of x-ray transmission in air over 3 meters at standard temperature and pressure, based on mass attenuation coefficients provided by NIST [15].

3.2 CdTe detector

A cadmium telluride (CdTe) detector was selected for the beamline because of its high efficiency over a wide range of energies, about 10-150 keV. The majority of the optics that will be measured on the beamline, including those discussed in Chapter 4, have energy response peaks falling in this range. For measurements below 10 keV, a silicon drift detector (SDD), which detects x-rays in the 1-25 keV range, was purchased. The use of the SDD is discussed in Appendix A, but was not used in this thesis work.

3.2.1 Theory of operation

When an x-ray interacts with the CdTe diode, it ionizes some of the atoms in the diode to produce electron-hole pairs. The number of pairs produced is proportional to the energy of the interacting x-ray. An applied electric field sweeps the electrons and positive ions to the anode and the cathode, respectively, producing a current pulse. A capacitor in the preamplifier integrates this current into an output voltage signal, and the shaping amplifier processes the voltage steps in this signal into shaped pulses with amplitudes proportional to the deposited energy. The detector's built-in

multichannel analyzer (MCA) sorts these shaped pulses into a histogram by peak amplitude.

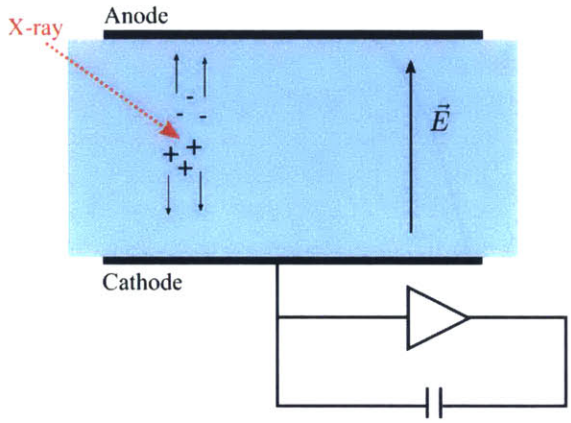

Figure 3-4: Cross-sectional geometry of the CdTe detector diode.

CdTe is a compound semiconductor material with high Z and a wide bandgap. This compound is a special case of the $Cd_{1-x}Zn_xTe$ (CZT) semiconductor which is commonly used in nuclear detection applications. The CdTe diode uses a planar geometry, with a uniform electric field between two parallel contacts, as shown in Fig 3-4.

When an electron-hole pair is created by an interacting x-ray, both types of charge carriers drift towards their respective contacts at a velocity proportional to the electric field strength. The constant of proportionality is known as the mobility, and is much higher for electrons than for the holes (positive ions) due to their smaller effective mass. Thus the electrons create a higher current over a shorter time than do the holes. In compound semiconductors, defects in the material created during the manufacturing process can cause the holes to become "trapped" before they reach the cathode. Because the hole lifetimes in these compounds are relatively small, some positive charge will be lost and the current induced in the cathode will be significantly reduced. This effect, known as charge trapping, leads to a significant amount of the counts falling in the exponential tail of the peak shape. This is especially true at higher energies, and must be accounted for during calibration (see Eq. 3.3). This effect is negligible in pure Si detectors due to low numbers of defects and long hole

lifetimes [25].

The Amptek X-123 CdTe detector selected for the beamline consists of a 1 mm thick CdTe diode behind a 4 mil (≈100 μm) beryllium protective window. The efficiency of the detector is proportional to the probability of a photon interacting in the diode material, given by

$$P = \left(e^{-\mu_{\text{dead}} t_{\text{dead}}}\right)\left(e^{-\mu_{\text{Be}} t_{\text{Be}}}\right)\left(1 - e^{-\mu_{\text{CdTe}} t_{\text{CdTe}}}\right), \tag{3.1}$$

where t_{Be}, t_{CdTe} and t_{dead} are the thicknesses of the Be window, the CdTe diode, and any dead, i.e. noninteracting, material (including the diode contacts), and μ_{Be}, μ_{CdTe} and μ_{dead} are the respective linear attenuation coefficients. On the low end of the energy spectrum, the efficiency is limited by the probability of x-rays being stopped by the Be window. On the high end, it is limited by the probability of x-rays passing through the CdTe diode material without interacting. Because CdTe has a relatively high linear attenuation coefficient compared to other detector materials such as silicon, its energy range is much larger, with $>$ 25% efficiency up to about 150 keV [26].

The single-pixel detector is not position sensitive, and has a large area (5 mm $\times$ 5 mm) compared to the point spread function of the optic. Therefore, to measure the point spread function, a set of caps with pinholes was manufactured to be placed over the end of the detector. The point spread function can be determined by measuring the amount of flux reaching the detector when pinholes of different sizes are placed over the window (see Sec. 4.1.2 for details of the measurement process). These pinholes are made of 0.5 mm thick tungsten and have diameters ranging from 0.01-5 mm.

3.2.2 Energy calibration

The data returned by the detector MCA takes the form of a number of counts in each MCA channel. To make use of this data, we must determine the relationship between MCA channel number and photon energy. This is achieved by using the detector to

Table 3.2: Spectral lines used in detector calibration. [4, 5]

Source Isotope	Spectral Line	Energy (keV)
^{57}Co	Fe $\gamma_{1,0}$	14.4
	Fe $\gamma_{2,1}$	122.1
	Fe $\gamma_{2,0}$	136.5
^{137}Cs	Ba K_α	32.2
	Ba K_β	36.4

measure a number of radioactive sources with known characteristic lines. The MCA channels in which these characteristic lines occur can be correlated with the known energies of these lines to determine the detector's calibration.

There exists a linear relationship between the energy E and MCA channel number n: $E = n/A + B$, where A is the system conversion gain in channels/keV, and B is the spectrum offset in keV. The system conversion gain is a product of three factors: the preamplifier conversion gain (mV/keV), the voltage amplifier gain (G, dimensionless) and the MCA conversion gain (channels/mV). The MCA conversion gain is given by the number of MCA channels in use (N) divided by the voltage corresponding to the peak channel [1]. Thus we can write the linear relationship as

$$E = \frac{n}{N \times G \times C} + B, \tag{3.2}$$

where C is a calibration constant that encompasses the unknowns in the hardware configuration, and is independent of the MCA and amplifier settings. By determining C, we can determine the channel-to-energy conversion for any values of G and N.

The detector was calibrated using two radioactive isotopes, ^{57}Co and ^{137}Cs. For each calibration spectrum, the sealed source was placed in front of the detector and a spectrum was obtained for 10 minutes. The peaks identified in each spectrum are listed in Table 3.2. To precisely locate the peaks, each spectral line was fit to a function of the form

$$I(n) = A \exp\left(\frac{\lambda}{2}(2\mu + \lambda\sigma^2 - 2n)\right)\left[1 - \mathrm{erf}\left(\frac{\mu + \lambda\sigma^2 - n}{\sqrt{2}\sigma}\right)\right], \tag{3.3}$$

where $I(n)$ is the intensity in channel number n, and A, λ, μ, and σ are fitting constants to be determined. This functional form results from the convolution of a Gaussian peak with an exponential tail caused by charge trapping effects. The fits were performed using a least squares method via the SciPy package for Python [18]. Once each peak was fit, numerical methods were used to identify the maximum of the fitted function. The channel number of this maximum and the energy corresponding to the peak were fit to a line of the form of Eq. 3.2. The full spectra and the linear fits are shown in Fig. 3-5.

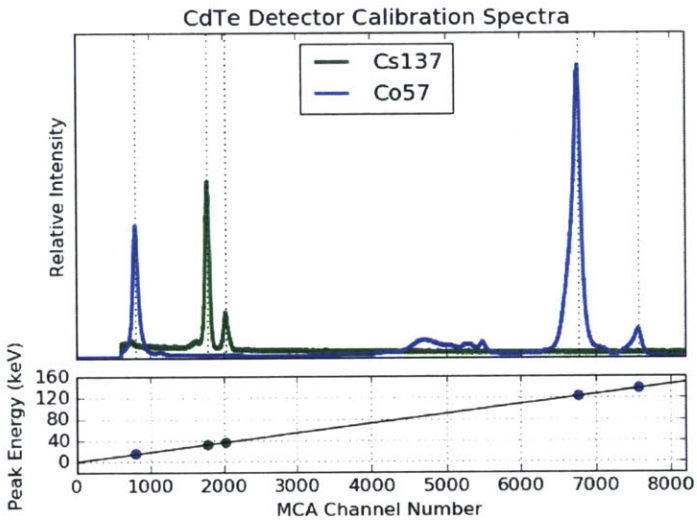

Figure 3-5: Spectra and linear fits for the CdTe detector. The amplifier gain was set to $G = 9.403$, and 8192 MCA channels were used for these spectra, the maximum available.

The results of the calibration are: $C_{\mathrm{CdTe}} = 7.18 \times 10^{-4}$ keV^{-1} and $B_{\mathrm{CdTe}} = -0.3$ keV. These calibration numbers are used for the measurements in Chapter 4.

3.3 Optic and detector mounts

The precise alignment required for measurement of these optics necessitates the use of precise, computer controllable motorized stages to manipulate the positioning of both the optic and detector. Seven stages with high-resolution stepper motors are in use in the beamline. Two rotational stages provide control of the pitch and yaw of

the optic, and two linear stages allow movement of the optic along the x and z axes (see Fig 3-6 for coordinate reference). Three linear stages under the detector mount allow alignment in the x, y and z directions.

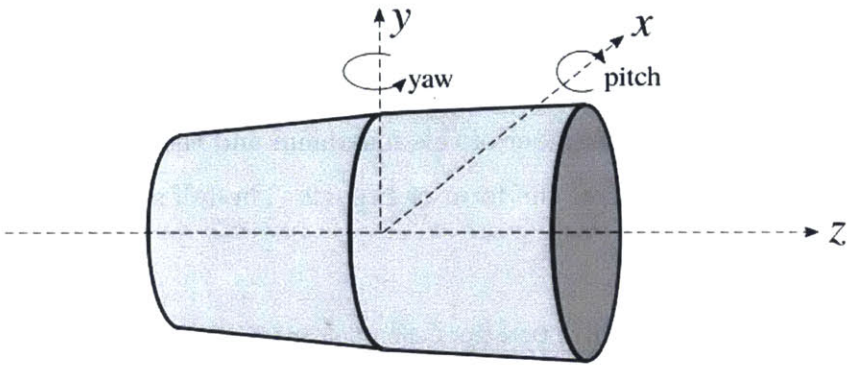

Figure 3-6: Illustration of the coordinate system used in alignment of the beamline. Stepper motor stages allow translation of the optic along x and z and rotation about the x (pitch) and y (yaw) axes.

A stainless steel structure is used for fixturing the optics to be placed on the beamline mount. In addition to holding the optic level and stationary, the mounting structure, shown in Fig. 3-7, also blocks the central portion of the straight-through beam. Photons that pass through the annulus of the structure are either focused by the optic or pass out of the range of the detector.

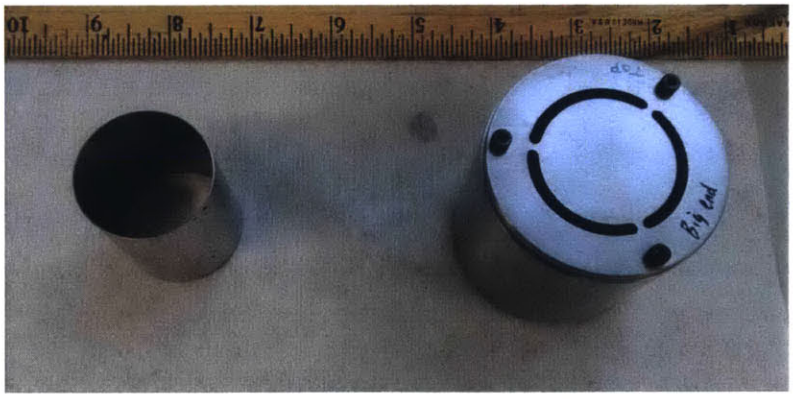

Figure 3-7: Left: One of the optics measured in this study, measuring about 1.75 inches long and 1.25 inches in diameter. Right: The stainless steel mounting structure designed for optics of this size, which holds the optic in place during alignment and measurement. The annulus of the structure allows x-rays to impinge on the optic while blocking the straight-through beam.

3.4 Control software

A dedicated software package was developed for this beamline to control the motorized stages and interface with the detector simultaneously for ease of alignment. Several scripts were also written to perform the data analysis. The software was written using the Python programming language, version 2.7. A Python library for communicating with the motorized stages via serial port was provided by the manufacturer. As no Python library was available for the detectors, one was written for this project using PySerial. The software built on top of these libraries provided two main functions: acquisition of a spectrum and motor scanning.

While a spectrum is being acquired, the software displays real-time data from the detector's built-in MCA. The previously determined detector calibration is used to convert the MCA data into a plot of counts versus energy. The software calculates the location and full width at half maximum (FWHM) of the largest peaks in the spectrum as it is acquired. Once acquisition is finished, the spectrum can be exported to a text file. This file also includes status information from the detector, such as its temperature, hardware gain and the various shaping parameters used by the preamplifier.

The beamline software's scanning capability consists of moving one or two stages over a given distance, while stopping at set increments along the way and acquiring a spectrum at each of these positions. This function is used primarily during the alignment of the optic and detector. For both single- and double-axis scans, a plot is displayed in real time showing the total number of counts detected at each location.

The user may define an energy region of interest (ROI) in the acquired spectra. For a multilayer coated optic, this function is used to monitor the energy range where the reflectivity peak is expected to occur, determined by the d-spacing of the multilayer film. If an ROI is defined before a scan, then the software will also plot the number of counts that occur in the ROI at each location.

The 2D scan is used to center the detector on the focal spot in the xy plane. The x and y stages on which the detector is mounted are scanned in a square grid pattern

and the results are displayed in real time in a "heat map" type plot. The software calculates the "center of mass" of the scan, the coordinates of which are defined as

$$(x_{\text{com}}, y_{\text{com}}) \equiv \frac{1}{\sum_{i,j=1}^{N} n_{ij}} \left(\sum_{i=1}^{N} x_i \sum_{j=1}^{N} n_{ij}, \sum_{j=1}^{N} y_i \sum_{i=1}^{N} n_{ij} \right), \tag{3.4}$$

where n_{ij} is the number of counts measured in the grid space located at (x_i, y_j). The results of a single motor scan or a 2D scan can be exported in the form of a set of text files, containing the spectrum acquired at each scan position.

3.5 Alignment procedure

Correct alignment of both the optic and detector is essential to accurate measurement of the optic's properties. In particular, the energy response is extremely sensitive to the grazing angle of the incident x-rays, so care must be taken to ensure that the optic is centered within the x-ray beam and that its axis is parallel to the beam path.

3.5.1 Initial visual alignment

The x-ray source is removed for the initial steps in the alignment. First, a laser beam is shone down the length of the beamline. The optic and detector are aligned with respect to the laser beam to ensure that they are collinear. The laser is then replaced with a fiber optic divergent white light source. The white light source is placed at the location where the x-ray tube's target will be mounted. With the optic flooded by visible light, two focal spots will be produced: one at the focal point of the optic, and one closer to the optic, made up of those photons which reflect only from the ellipsoid portion of the optic. This ellipsoid focus is brighter than the optical focus and is useful for the alignment process.

A piece of paper or other non-reflective surface is placed at the ellipsoid focus. The image that appears is shown in Fig. 3-8. When the optic is mis-aligned, the image consists of an asymmetrical ring with a bright spot near the edge, as shown in Fig. 3-8a. As the pitch and yaw of the optic are adjusted, the image becomes a

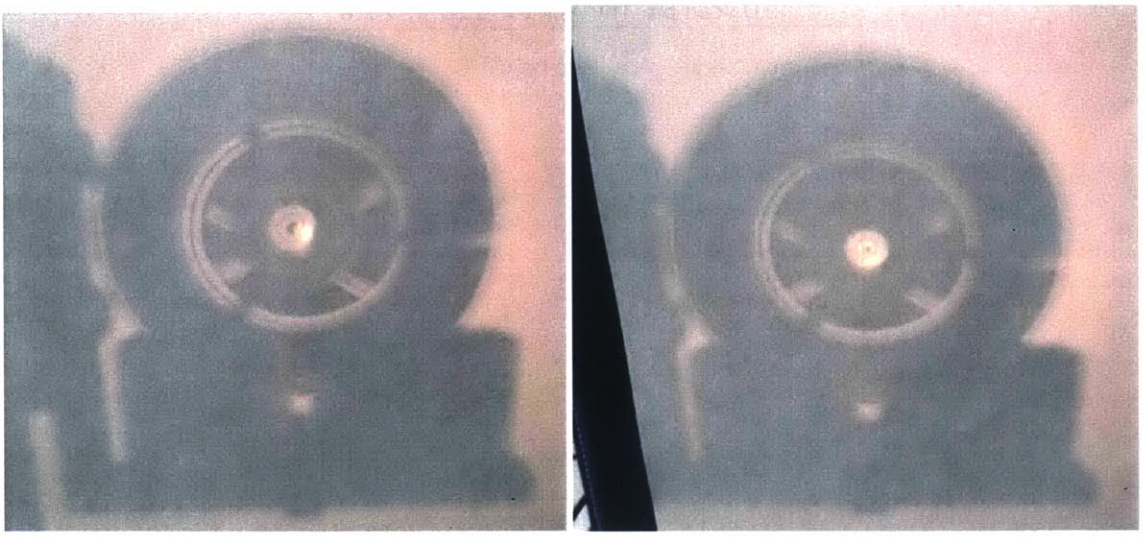

(a) Off-axis alignment (b) On-axis alignment

Figure 3-8: Illustration of the alignment of the optic with respect to the beam path using visible light from a fiber optic source. The small center ring is formed by the single-bounce photons, and the outer ring is straight-through beam that passes through the annulus of the structure and is not reflected by the optic. An asymmetric single-bounce image indicates that the optic is off-axis, while a symmetric ring indicates proper on-axis alignment.

symmetric ring, shown in Fig. 3-8b, indicating that the optic is roughly on-axis.

3.5.2 Alignment with x-ray source

After the visual alignment, the x-ray source is re-mounted as shown in Fig. 3-1 and the power supply is ramped up to the desired settings. In order to more precisely locate the focal spot, the detector is scanned in a square $N \times N$ grid about the location determined by the initial alignment, and moved to the center of mass of the scan (see Eq. 3.4). Each grid space is 5 mm $\times$ 5 mm, the approximate size of the detector diode area. Typically a scan of $N = 3$ or $N = 5$ is sufficient to locate the focal spot.

Next, an energy ROI is defined in the energy band where the reflectivity peak is expected, and the orientation of the optic is aligned. The pitch and yaw of the optic are alternately scanned from $-0.3°$ to $0.3°$ in increments of $0.05°$. After each scan, the optic is moved to the location which has the most counts in the ROI. An example plot from this process is shown in Fig. 3-9. This scan is then reduced to $-0.2°$ to $0.2°$

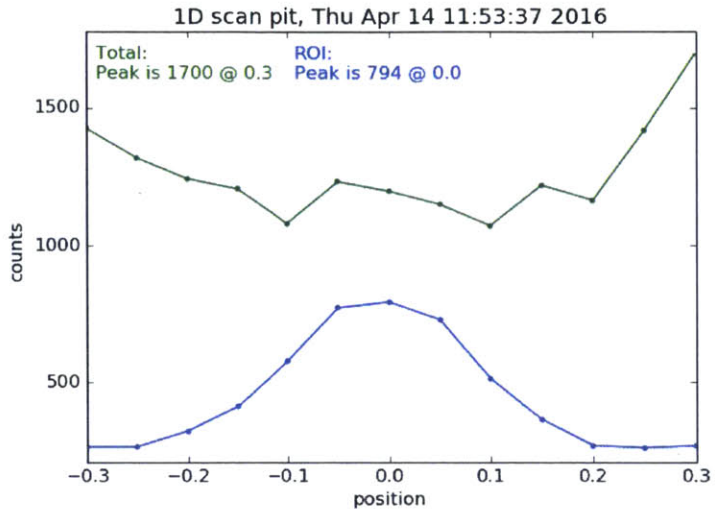

Figure 3-9: The plot produced by the software during the alignment of the optic's pitch coordinate, showing the total number of counts (of all energies) at each location (green) and the number of counts in the ROI (blue). The position on the x-axis has units of degrees. This plot was produced with a dwell time of 3 seconds at each location. The plot of ROI counts has a peak around 0° pitch, indicating a good alignment.

in increments of 0.025°, and finally −0.1° to 0.1° in increments of 0.01°.

Now that the optic has been aligned, the detector alignment with respect to the focal spot is further refined. The detector alignment grid scan described above, with a 5 mm × 5 mm grid spacing, is repeated to relocate the focus. Then the detector alignment is refined by repeating the scan with smaller grid spacings of 3 mm × 3 mm, 2 mm × 2 mm, and finally 1 mm × 1 mm, each time with the pinhole cap of the corresponding diameter placed on the detector. An example of the figure displayed by the software during this portion of the alignment is shown in Fig. 3-10.

The last step before a measurement can be taken is to align the detector in the z direction (along the beam). The z location of the focus is the point where the beam is smallest in diameter. This location is identified by moving the detector from -10 mm to +10 mm in increments of 2.5 mm. At each location, the half-power diameter (HPD) is measured using the pinholes. The details of this calculation are given in Sec. 4.1.2. At the end of this scan, the detector is moved to the point with the lowest HPD, and the final data acquisition is begun.

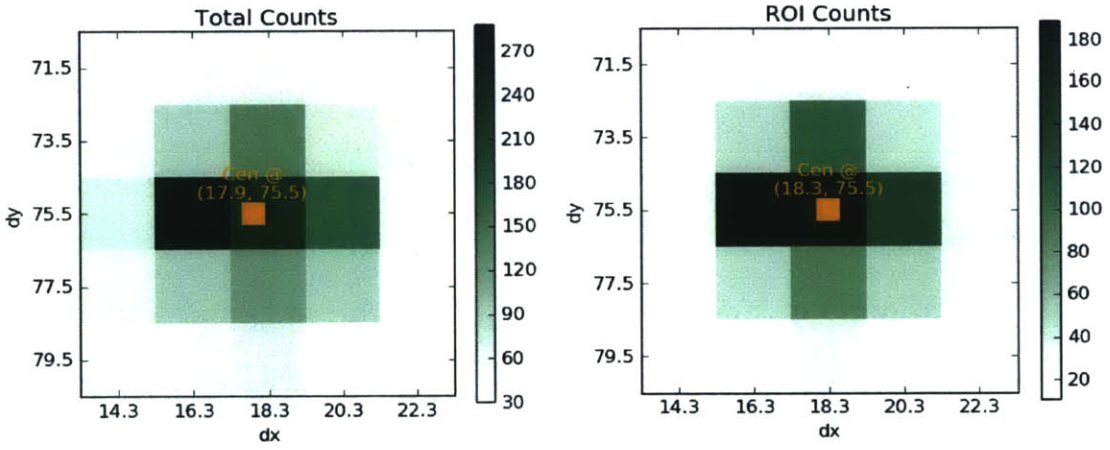

Figure 3-10: The grid display produced by the software during the final alignment of the detector with the focal spot of the x-rays. The heat maps of both total spectrum counts and ROI counts are shown, and the center of mass of each scan is indicated with an orange box. This data was acquired with a 2 mm pinhole over the detector, and a 2 mm step size. A 5 second dwell time was used.

Chapter 4

Measurement procedures and results

The first section of this chapter discusses the process of acquiring data from the beamline and processing it into plots of reflectivity versus energy, which can be compared with theoretical models. In section 4.2, I present the results of this measurement procedure on two optics fabricated at CfA and compare the acquired data with models created using IMD.

4.1 Measurement procedures

4.1.1 Reflectivity

Once the optic and detector are aligned according to Sec. 3.5, a spectrum is obtained with the optic in place over a sufficiently long period of time to obtain a significant number of counts. We have found that 10 minutes provides enough flux when using a current of 0.2 mA or more in the x-ray tube. The optic is then removed and a "background" spectrum is acquired over the same time period. To acquire the background spectrum, it is necessary to place a pinhole over the detector so that the collecting area of the detector is well defined. This collecting area will be compared with the collecting area of the optic in the calculation of reflectivity.

In each energy bin of the resulting spectra, the square of the reflectivity of the optic surface, R^2, is related to the ratio between the reflection from the optic and the

beam intensity entering the optic at that energy. This ratio is proportional to R^2 as opposed to simply R because the photons being measured in the optic response are doubly reflected, first from the hyperboloid and then from the ellipsoid portion of the optic.

The background spectrum has the same form as the beam entering the optic, but its magnitude must be rescaled. When taking the optic spectrum, we are collecting x-ray photons that have traveled the distance from the source to the optic ($d_{\text{optic}} = 0.6$ m) and are then focused onto the detector. In the background spectrum, the beam has spread out for the full distance from the source to the detector ($d_{\text{detector}} = 3.0$ m). Because of the inverse square relationship between distance and intensity for a spherical wave, we must multiply background spectrum by a factor of $d^2_{\text{detector}}/d^2_{\text{optic}}$ in order for it to be representative of the beam entering the optic.

We must also account for the fact that the optic and the detector have different collecting areas, requiring a multiplicative factor of $A_{\text{detector}}/A_{\text{optic}}$ on the background spectrum. The collecting area of the detector is simply defined by the size of the pinhole used in collecting the background, $A_{\text{detector}} = \pi r^2_{\text{pinhole}}$. The collecting area of the optic, A_{optic}, is discussed in Sec 2.2.

In sum, the reflectivity R_i in energy bin i is characterized by

$$R_i^2 = \left(\frac{O_i}{B_i}\right)\left(\frac{\pi r^2_{\text{pinhole}}}{A_{\text{optic}}}\right)\left(\frac{d_{\text{optic}}}{d_{\text{detector}}}\right)^2, \tag{4.1}$$

where O_i and B_i are the number of counts in energy bin i in the optic and background spectra, respectively.

4.1.2 Resolution

The half-power diameter (HPD) of the optic, which is a measure of its resolving power, is determined by measuring the intensity reaching the detector when it is obscured by caps with pinholes of various diameters. Assuming that the beam has a Gaussian intensity profile, we can model the incident power enclosed by a pinhole of diameter

D as

$$P(D) = \int_0^{2\pi} d\theta \int_0^{D/2} r dr A \exp\left(\frac{-r^2}{2\sigma^2}\right)$$
$$= 2\pi\sigma^2 A \left[1 - \exp\left(\frac{D^2}{8\sigma^2}\right)\right], \tag{4.2}$$

where A and σ are parameters to be determined by fitting. Then the HPD, where $P(d) = P_{\max}/2$, is given by

$$D_{\text{HPD}} = 2\sigma\sqrt{2\log 2}. \tag{4.3}$$

To obtain a measurement of the true spatial resolution of the optic, we must separate the effects of this resolution on the measured HPD from the effect of the finite size of the source. The optic's spatial resolution is given by

$$D_{\text{res}} = \sqrt{D_{\text{HPD}}^2 - D_{\text{source}}^2}, \tag{4.4}$$

where D_{source} is the diameter of the focal spot inside the x-ray source.

4.2 Results

Two x-ray optics which were recently fabricated at CfA, called R3 and R6, were measured using the beamline. These optics are prototypes for a diagnostic tool for laser plasma fusion experiments. These diagnostic tools would function as a filter to discern characteristic emissions from molybdenum at 17.5 keV. The reflective surface of the optics are coated with silicon-tungsten (SiW) multilayers. Both optics were replicated from the same mandrel and thus have the same macroscopic dimensions. The graze angle varies from 0.49° to 0.51° along the length of the optic, and for the models presented here we use the average graze angle of 0.50°.

For both optics, the measured energy responses were compared with models created with IMD. The point-spread function of each optic was also measured and used to calculate the optic's spatial resolution. Both measurements consist of a background spectrum and an energy response spectrum, each taken over a period of 10 minutes.

The Cr x-ray source was used for all measurements, with a 30 kV high voltage bias applied.

4.2.1 Optic R3

The first x-ray optic measured in this study, R3, is coated with a 45 bilayer SiW film. The thickness parameters used in fabrication of the multilayer film of R3 are shown in Table 4.1.

Table 4.1: Deposition thickness parameters of the R3 SiW multilayer film

Parameter	**Value**
Number of bilayers (N)	45
Bilayer thickness (d)	50.00 Å
Layer thickness ratio (Γ)	0.24
W layer thickness (d_{W})	38.00 Å
Si layer thickness (d_{Si})	12.00 Å

Reflectivity

The raw optic reflection data and the background spectrum are plotted together in Fig. 4-1. The multilayer response peak appears at around 15 keV in the optic reflection data, and a portion of the initial reflectivity plateau, discussed below, is visible near 8 keV. This raw data was used to calculate the reflectivity of the optic according to Eq. 4.1. The calculated reflectivity is shown in Fig. 4-2 and compared with two different models of the SiW multilayer created using IMD. Both models were created using the parameters listed in Table 4.2 for the characteristics of the carbon release layer, platinum layer and NiCo substrate and the microroughness at the multilayer interfaces.

In both plots in Fig. 4-2, the initial reflectivity plateau is visible in the models for energies below about 9 keV. This plateau is due to reflection of low-energy photons off the top layer of tungsten in the multilayer. In the measured reflectivity data, the plateau manifests as a peak around 8 keV. As discussed in Sec. 3.1, the portion of the

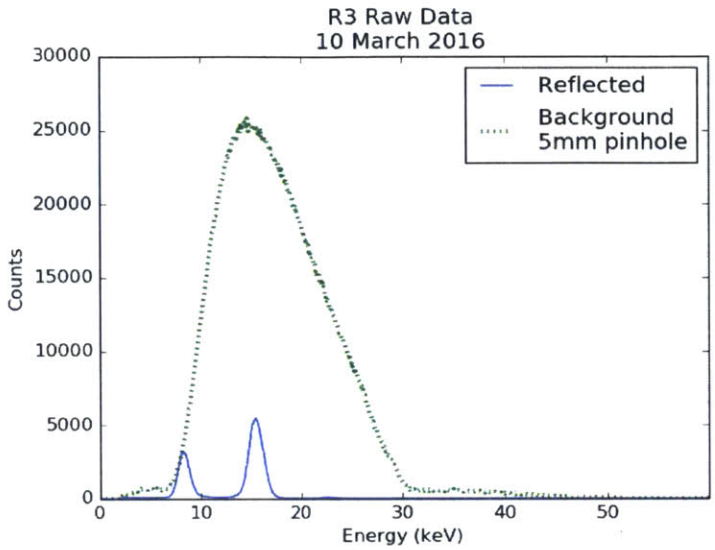

Figure 4-1: Flux versus energy with and without the R3 optic in the beamline. The background spectrum shows the output of the x-ray source, with a 5 mm pinhole placed over the detector window. The blue solid line shows data taken with the optic placed in the beamline. The x-ray tube current was set to 0.3 mA for both measurements.

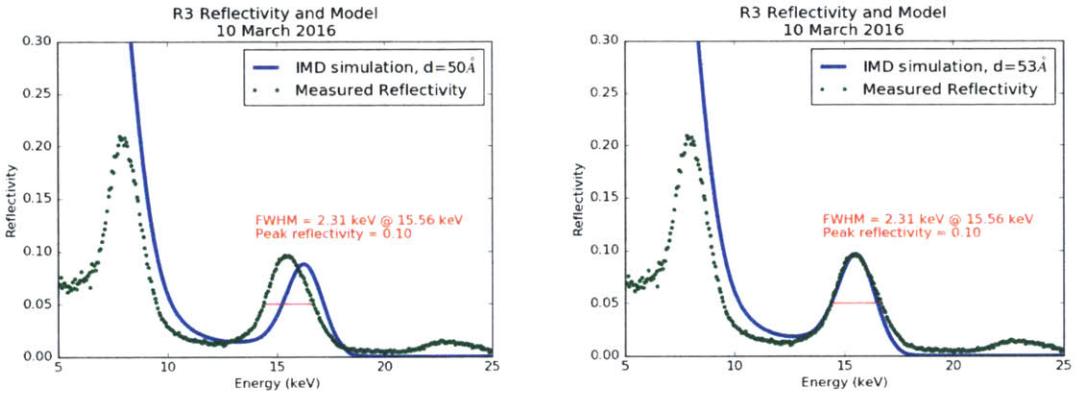

(a) Model using multilayer deposition parameters

(b) Model using increased d-spacing

Figure 4-2: Reflectivity versus energy for optic R3 is shown in both plots, calculated from the data shown in Fig. 4-1 using Eq. 4.1. The measured reflectivity has a maximum of 0.10 at 15.56 keV, with a FWHM of 2.31 keV. Two IMD models are plotted for comparison. In (a), the model uses the deposition parameters from Table 4.1 for the SiW multilayer. In (b), the model uses a SiW multilayer with an increased d-spacing, with parameters given in Table 4.3. Both models use the parameters listed in Table 4.2 for the remaining film characteristics.

Table 4.2: IMD parameters for models of optic R3. See Tables 4.1 and 4.3 for the thickness parameters of the SiW multilayer used in the two models.

Layer number	**Material**	**Parameters**
1	C	$z = 40.00$ Å, $\sigma = 9.00$ Å
2	Si	$z = 40.00$ Å, $\sigma = 9.00$ Å
3	Si/W multilayer	$\sigma = 9.00$ Å
4	Pt	$z = 20.00$ Å, $\sigma = 9.00$ Å
Substrate	$Ni_{85}Co_{15}$	$\rho = 8.908$ g/cm^3, $\sigma = 9.00$ Å
Detector energy resolution	ΔE	0.75 keV
Grazing angle	θ	0.50°

plateau below about 7.5 keV is cut off due to the absorption of these photons in air over the length of the beamline.

The first model, shown in Fig. 4-2a, uses the deposition parameters listed in Table 4.1 for the SiW multilayer film. This model predicts a reflectivity peak that is similar in shape and height to the data, but shifted toward higher energies. This indicates that the actual thickness of the bilayers may be slightly greater than the parameters used for deposition.

A second model was created using thicker bilayers, shown in Fig. 4-2b. This model uses a bilayer thickness of $d = 53$ Å instead of $d = 50$ Å. The multilayer parameters for this model are listed in Table 4.3. This model more accurately corresponds with the location of the peak in the data, indicating that the actual multilayer film deposited on the mandrel has a bilayer thickness closer to 53 Å. The discrepancy between this model and the deposition parameters is possibly caused by an error in the estimated sputtering rate during the deposition of the multilayer.

Resolution

The resolution of the R3 optic was determined by measuring the enclosed power for various pinhole diameters and fitting the data to a function of the form of Eq. 4.2. This data and the fitted model is shown in Fig. 4-3. The result of the fit is an HPD of 2.981 mm. To find the spatial resolution, we insert this HPD as well as the x-ray

Table 4.3: Model thickness parameters of the R3 SiW multilayer film with increased d-spacing

Parameter	Value
Number of bilayers (N)	45
Bilayer thickness (d)	53.00 Å
Layer thickness ratio (Γ)	0.24
W layer thickness (d_{W})	40.28 Å
Si layer thickness (d_{Si})	12.72 Å

tube's focal spot area into Eq. 4.4. According to the manufacturer test data sheet for the Cr tube, the focal spot measures 206.3 μm in diameter. The result is a spatial resolution of 2.974 mm for this optic.

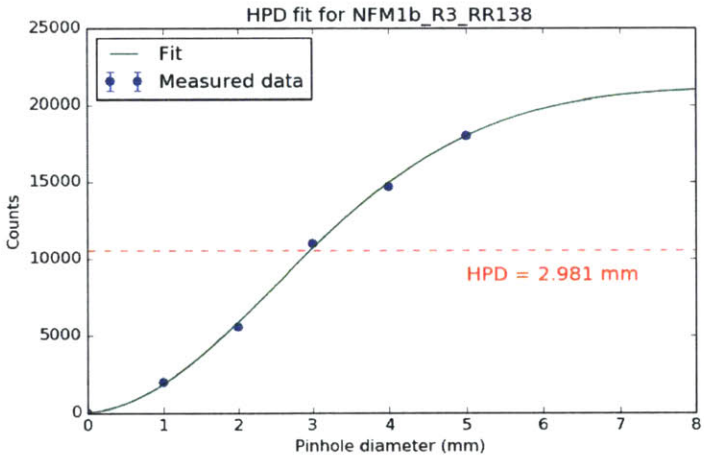

Figure 4-3: Power spectrum fit for x-ray optic R3. Each data point corresponds to a spectrum taken over a period of 30 seconds.

4.2.2 Optic R6

The second optic measured, R6, has a 20 bilayer SiW coating, fabricated using the parameters shown in Table 4.4.

Reflectivity

The raw data, consisting of the reflection data from the optic and the background spectrum, are shown plotted on the same axes Fig. 4-4. Two peaks are visible in the

Table 4.4: Deposition thickness parameters for R6 SiW multilayer film

Parameter	Value
Number of bilayers (N)	20
Bilayer thickness (d)	37.20 Å
Layer thickness ratio (Γ)	0.64
W layer thickness (d_{W})	13.39 Å
Si layer thickness (d_{Si})	23.81 Å

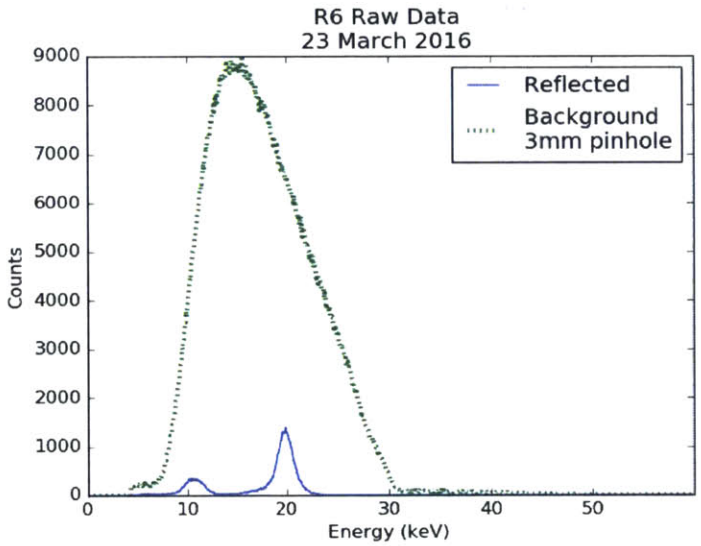

Figure 4-4: Flux versus energy with and without the R6 optic in the beamline. A 3 mm pinhole was placed over the detector for the background spectrum. Both measurements were taken with an x-ray tube current of 0.2 mA.

optic reflection data, one at 20 keV and one at about 11 keV. The higher peak at 20 keV is the multilayer response, and the 11 keV peak is the portion of the initial reflectivity plateau which is transmitted through the 3 meters of air in the beamline.

From this data, the reflectance of the optic was calculated using Eq. 4.1. This data is compared with two different models created using IMD, shown in Fig. 4-5. The parameters for both of these models which account for the estimated microroughess in the multilayer and other layers in the film are listed in Table 4.5. As shown in the figure, the peak reflectivity of this optic is less than that of R3, which is expected due to the reduced number of bilayers ($N = 20$ vs $N = 45$).

The model shown in Fig. 4-5a uses the deposition parameters for the thickness

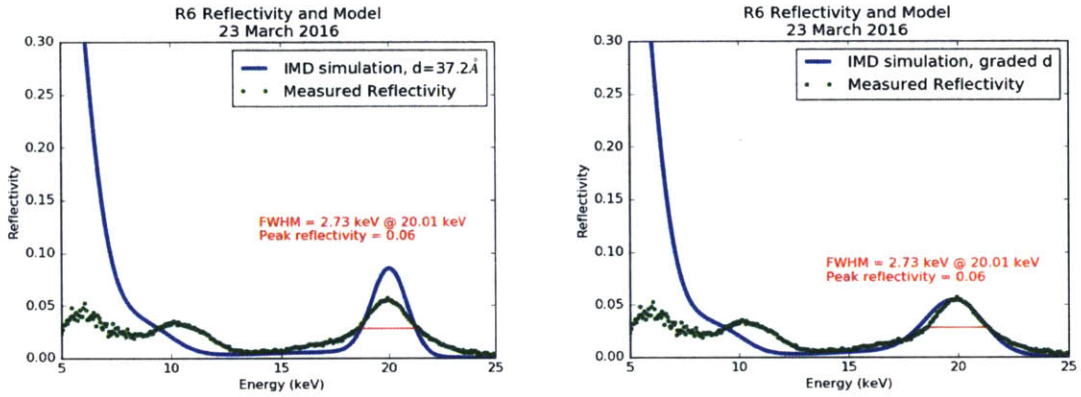

(a) Model using multilayer deposition parameters

(b) Model using graded layer thickness

Figure 4-5: Reflectivity versus energy for optic R6 is shown in both plots. The calculated reflectivity has a maximum of 0.06 at 20.01 keV, with a FWHM of 2.73 keV. Also shown in the plots are two IMD models. (a) shows a model using the deposition parameters from Table 4.4 for the SiW multilayer. (b) shows a model with a graded thickness of the SiW multilayer, characterized by Table 4.6. Both models use the parameters in Table 4.5 for the remaining characteristics of the film.

Table 4.5: IMD parameters for models for optic R6. See Tables 4.4 and 4.6 for the thickness parameters of the SiW multilayer used in the two models.

Layer number	**Material**	**Parameters**
1	C	$z = 40.00$ Å, $\sigma = 9.00$ Å
2	Si	$z = 40.00$ Å, $\sigma = 9.00$ Å
3	Si/W multilayer	$N = 20$, $\sigma = 9.00$ Å
4	Pt	$z = 20.00$ Å, $\sigma = 9.00$ Å
Substrate	$Ni_{85}Co_{15}$	$\rho = 8.908$ g/cm^3, $\sigma = 9.00$ Å
Detector energy resolution	ΔE	0.50 keV
Grazing angle	θ	0.75°

of the SiW multilayer, listed in Table 4.4. As shown in the plot, the location of the optic's reflectivity peak is well matched by the model, with both centering around 20 keV. However, the optic's reflectivity peak is considerably shorter and broader than the prediction of the model. This could indicate that the thicknesses of the layers that make up the multilayer are not uniform, causing a greater band of energies to be reflected.

To test this hypothesis, a model was created using a variable layer thickness for

Table 4.6: Depth-graded model parameters for R6 SiW multilayer film. Graded parameters vary linearly from top to bottom of the multilayer film.

Parameter	Value
Number of bilayers (N)	20
Bilayer thickness (d)	Graded: 33.21 to 41.48 Å
Layer thickness ratio (Γ)	Variable: 0.66 to 0.62
W layer thickness (d_{W})	Graded: 11.40 to 15.58 Å
Si layer thickness (d_{Si})	Graded: 21.81 to 25.90 Å

the SiW bilayers, shown in Fig. 4-5b. In this model, the thickness of each bilayer varies linearly from $d = 33.21$ Å at the top of the film to $d = 41.48$ Å at the bottom. As the plot shows, this model fits the height and shape of the peak much better than the first model, indicating that a variable layer thickness is a reasonable explanation for the broadening of the peak in the reflectivity data. This is likely caused by a sputtering deposition rate that varies throughout the deposition process.

For both plots in Fig. 4-5, the initial reflectivity plateau of the data is shifted toward higher energies than that of the model. It is not yet understood why this occurs, but may be due to an error in alignment causing a change in the grazing angle of the reflected x-rays. This feature occurs in all of the multiple data sets taken on this optic, and further investigation will be needed to understand what aspect of the alignment could be causing it.

Resolution

As shown in Fig. 4-6, the HPD obtained from the fitted data for optic R6 is 3.074 mm. Plugging into Eq. 4.4, we obtain a value of 3.067 mm for the spatial resolution. This indicates that the figure of this optic is slightly poorer than that of R3, possibly caused by increased stress on the NiCo shell during fabrication, resulting in deformation of the optic.

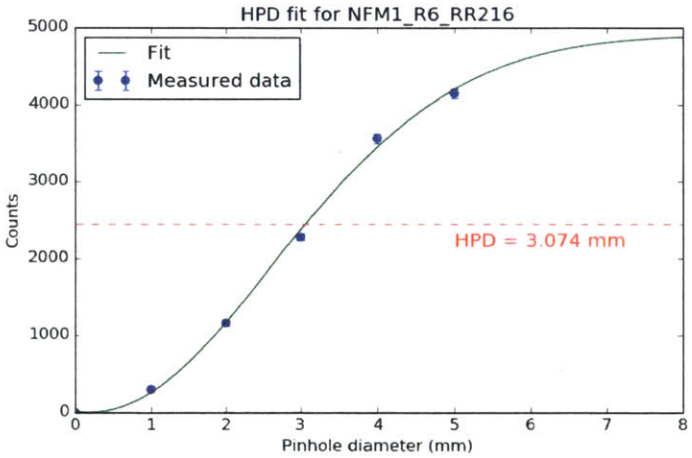

Figure 4-6: Power spectrum fit for x-ray optic R6. Each data point was acquired over a 30 second period.

Chapter 5

Conclusions

This thesis presented the development of an in-house beamline system for measurement of x-ray and neutron optics fabricated at the CfA. These optics have numerous applications for imaging in the fields of fusion diagnostics, planetary science, medical research and neutron science. The construction of a measurement apparatus at CfA will aid in streamlining the process of fabricating and developing these optics.

In Chapter 4, we presented initial measurement results from the beamline on two x-ray optics fabricated at CfA. Measurements of the optics' energy responses agree qualitatively with model predictions in both cases, but some discrepancies were noted which require further investigation. As show in Fig. 4-2a, the reflectivity peak of optic R3 is shifted slightly toward lower energies compared to the prediction of a model based on the deposition parameters used in coating this optic. This is likely an indication that the actual thicknesses of the bilayers in the coating are greater than the intended thicknesses. Fig. 4-2b shows that a model using greater thicknesses is a significantly better match to the reflectivity data. Work is ongoing to characterize the actual layer thicknesses of this optic using transmission electron microscopy.

The reflectivity peak of R6 is significantly broadened with respect to what is expected based on the deposition parameters, as shown in Fig. 4-5a. This may be an indication of nonuniform thickness of the bilayers that make up the multilayer film, as demonstrated by the model in Fig. 4-5b. In addition, the portion of the initial reflectivity plateau which is visible in the measured response is shifted from

where it is expected to appear, which may be caused by improper alignment. We are continuing to refine the alignment process to determine the origin of this discrepancy.

These optics were both fabricated as prototypes for filtering diagnostic tools for a laser plasma fusion experiment. These tools require a narrow passband around the energy of the molybdenum Kα line, 17.5 keV. The first optic fabricated in this series, R3, has a reflectivity peak at 15.5 keV, too low to reflect the Mo Kα line. The layer thickness was decreased for R6 in an attempt to shift the reflectivity peak to higher energies by decreasing the sputter time for each bilayer. However, the layer thicknesses were decreased too much, so that the reflectivity peak of R6 is too high in energy, at 20 keV. The calibration of the sputtering rate for Si and W in the chambers at CfA is being assessed as we move toward the goal of producing an optic with a narrow reflectivity peak at 17.5 keV. Fine-tuning the parameters of the sputtering process may also allow us to increase the reflectivity of the optics by reducing microroughness and adding more bilayers to the film.

The models used to predict the responses of these optics based on coating parameters were created using the IMD software package [31]. While IMD is a useful tool for a prediction of the reflectivity of multilayer coated flat substrates, it was not designed for Wolter optics, in which the photons are doubly reflected and the graze angle varies slightly. The models in Chapter 4 use the average graze angle of 0.5°, but the actual graze angle of the optic varies from 0.49° to 0.51° along the length of the optic. We are now developing new simulations that account for the range of graze angles of the reflected photons, and we expect that more advanced simulations will better predict the reflectance peaks of these optics.

Continued development on the beamline will include implementation of a command-line user interface for the software controlling the detectors and motorized stages. A user-friendly interface will open up its functionality to users without prior knowledge of the Python programming language.

Other ongoing work at the CfA includes the development of optic fabrication technologies that will further decrease the mass and thickness of the optic shells using new materials and deposition processes. These future investigations will be

greatly aided by the addition of this beamline to the measurement facilities available at the CfA.

Appendix A

Low energy x-ray measurement

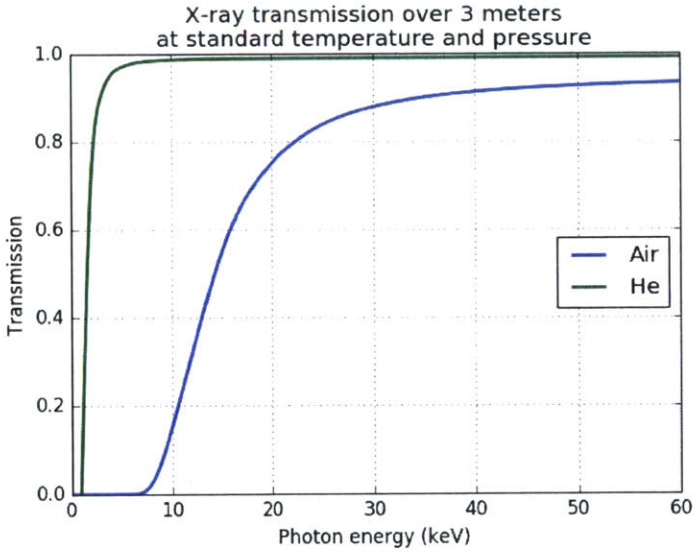

Figure A-1: A plot of the x-ray transmission in air and in helium over the 3 meter length of the beamline. Based on mass attenuation coefficients provided by NIST [15].

As shown in Fig. A-1, for x-rays with an energy below 9 keV, about 90% of the intensity is absorbed in air over the 3 meter length of the beamline, making replacement of the air with another, less absorbing gas essential for measurements below this energy. Helium makes a good choice for this application due to its low x-ray attenuation coefficient and low density at atmospheric pressure. For future investigations in the low energy regime, we will be sealing the PVC pipes used for shielding and pumping helium in to replace the air.

In addition to reducing the attenuation, a different detector must be used for low energy investigations. While the efficiency of the CdTe detector begins to drop off for energies below 10 keV, a silicon drift detector (SDD) has greater than 25% efficiency in the 1-25 keV range [2].

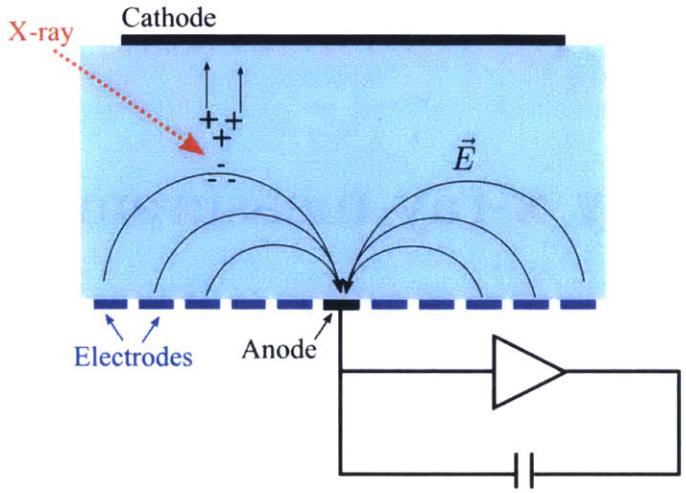

Figure A-2: Silicon drift detector geometry

The improved energy resolution and lower noise in the low energy range is largely due to the unique diode shape of the SDD. Instead of a planar anode, the SDD uses a small anode surrounded by negatively charged electrodes, shown in Fig A-2. The electric field guides electrons to the small anode area, while holes drift toward the planar cathode. This arrangement significantly reduces voltage noise by reducing the capacitance of the detector area [3]. In addition, the SDD has a thinner Be window, 0.5 mil, to allow transmission of lower energy photons into the diode volume. However, because silicon has a lower attenuation coefficient, the upper limit of the SDD's energy range (25 keV) is much lower than that of CdTe detectors (150 keV).

The SDD was calibrated in the same manner as the CdTe detector (Sec. 3.2.2), with the addition of a ^{55}Fe sealed source for calibration of the low energy regime. The characteristic lines used are listed in Table A.1. A plot for the calibration of the SDD is shown in Fig. A-3. The fit gives a calibration constant of $C_{\mathrm{SDD}} = 3.16 \times 10^{-3}$ keV^{-1} and an energy offset of $B_{\mathrm{SDD}} = -1.78 \times 10^{-2}$ keV. This calibration data will be used for future low-energy measurements taken with the SDD.

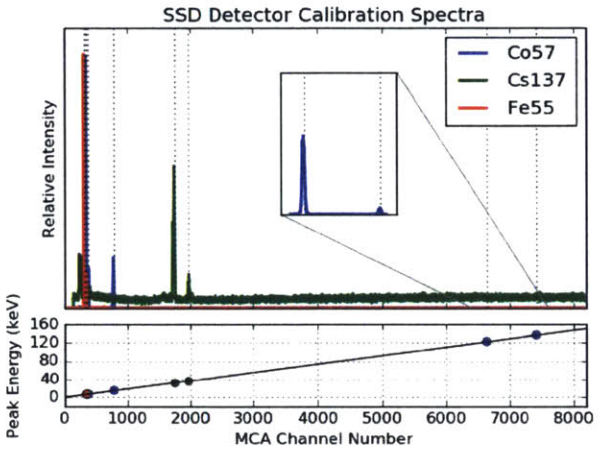

Figure A-3: Spectra and linear fits for the SDD. The amplifier gain was set to $G = 2.102$, and 8192 MCA channels were used.

Source Isotope	**Spectral Line**	**Energy (keV)**
^{55}Fe	Mn K_α	5.9
	Mn K_β	6.5
^{57}Co	Fe $\gamma_{1,0}$	14.4
	Fe $\gamma_{2,1}$	122.1
	Fe $\gamma_{2,0}$	136.5
^{137}Cs	Ba K_α	32.2
	Ba K_β	36.4

Table A.1: Spectral lines used in silicon drift detector calibration. [4, 5]

Bibliography

[1] Amptek, Inc., Bedford, MA. *Amptek Silicon Drift Detectors (AN-SDD-003).*

[2] Amptek, Inc., Bedford, MA. *Complete X-Ray Spectrometer with Silicon Drift Detector (SDD): User Guide and Operating Instructions, Rev A6.*

[3] Amptek, Inc., Bedford, MA. *Complete X-Ray Spectrometer with Silicon Drift Detector (SDD): User Guide and Operating Instructions, Rev A6.*

[4] M.-M. Bé, V. Chisté, C. Dulieu, E. Browne, C. Baglin, V. Chechev, N. Kuzmenko, R. Helmer, F. Kondev, D. MacMahon, and K.B. Lee. *Table of Radionuclides*, volume 3 of *Monographie BIPM-5.* Bureau International des Poids et Mesures, Pavillon de Breteuil, F-92310 Sèvres, France, 2006.

[5] M.-M. Bé, V. Chisté, C. Dulieu, E. Browne, V. Chechev, N. Kuzmenko, R. Helmer, A. Nichols, E. Schönfeld, and R. Dersch. *Table of Radionuclides*, volume 1 of *Monographie BIPM-5.* Bureau International des Poids et Mesures, Pavillon de Breteuil, F-92310 Sèvres, France, 2004.

[6] N.F. Brejnholt, T.A. Decker, R. M. Hill, H. Chen, G. J. Williams, J. Park, J. B. Alameda, M. Fernández-Perea, M. J. Pivovaroff, R. Soufli, M.-A. Descalle, J. Peebles, and S. M. Kerr. Reflective multilayer optic as hard x-ray diagnostic on laser-plasma experiment. *Review of Scientific Instruments*, 86(013110), 2015.

[7] B. D. Cullity. *Elements of X-Ray Diffraction.* Addison-Wesley, Reading, Massachusetts, second edition, 1978.

[8] D. E. Engelhaupt, B. D. Ramsey, S. L. O'Dell, W. D. Jones, and J. K. Russell. New alloys for electroformed replicated x-ray optics. In R. B. Hoover and A. B. Walker, editors, *X-Ray Optics, Instruments, and Missions IV*, volume 4138 of *Proc. SPIE*, pages 154–163, November 2000.

[9] R. Giacconi. The Einstein X-ray Observatory. *Scientific American*, 242:80–85, February 1980.

[10] D.J. Griffiths. *Introduction to Electrodynamics.* Addison-Wesley, second edition, 2012.

[11] M. V. Gubarev, B. Khaykovich, B. Ramsey, D. Moncton, V. E. Zavlin, K. Kilaru, S. Romaine, R. E. Rosati, R. Bruni, L. Robertson, L. Crow, H. Ambaye, and V. Lauter. From x-ray telescopes to neutron focusing. In *Society of Photo-Optical Instrumentation Engineers (SPIE) Conference Series*, volume 8147 of *Proceedings of the SPIE*, page 81470B, September 2011.

[12] Fiona A. Harrison, W. Rick Cook, Karl Forster, Brian W. Grefenstette, Kristin K. Madsen, Peter H. Mao, Hiromasa Miyasaka, William W. Craig, Michael J. Pivovaroff, Finn E. Christensen, and et al. The nuclear spectroscopic telescope array (NuSTAR) high-energy x-ray mission. *Astrophysical Journal*, 770(2), Jun 2013.

[13] Charles Hockin. On the estimation of aperture in the microscope. *Journal of the Royal Microscopic Society, Ser. II*, 4:337–347, 1884.

[14] J. Hong and S. Romaine. Miniature lightweight X-ray optics (MiXO) for surface elemental composition mapping of asteroids and comets. *Earth, Planets, and Space*, 68:35, February 2016.

[15] J. H. Hubbell and S. M. Seltzer. *Tables of X-Ray Mass Attenuation Coefficients and Mass Energy-Absorption Coefficients.* National Institute of Standards and Technology, Gaithersburg, MD., 2004.

[16] Adrian Ivan. *Fabrication and Characterization of Multilayers for Focusing Hard X-Ray Optics.* PhD thesis, Massachusetts Institute of Technology, June 2002.

[17] F. Jansen, D. Lumb, B. Altieri, J. Clavel, M. Ehle, C. Erd, C. Gabriel, M. Guainazzi, P. Gondoin, R. Much, R. Munoz, M. Santos, N. Schartel, D. Texier, and G. Vacanti. XMM-Newton observatory. I. the spacecraft and operations. *Astronomy and Astrophysics*, 365:L1–L6, January 2001.

[18] Eric Jones, Travis Oliphant, Pearu Peterson, et al. SciPy: Open source scientific tools for Python, 2016. Version 0.17.0.

[19] Paul Kirkpatrick and A. V. Baez. Formation of optical images by x-rays. *J. Opt. Soc. Am.*, 38(9):766–774, Sep 1948.

[20] R. Maruyama, D. Yamazaki, T. Ebisawa, M. Hino, and K. Soyama. Development of neutron supermirrors with large critical angle. *Thin Solid Films*, 515:5704–5706, 2007.

[21] L. Névot and P. Croce. Caractérisation des surfaces par réflexion rasante de rayons X. Application à l'étude du polissage de quelques verres silicates. *Revue de Physique Appliquee*, 15(3):761–779, 1980.

[22] Oxford Instruments, Scotts Valley, CA. *Radiation Shielded X-ray Tube, Jupiter 5000 Series Technical data sheet*, 2015. This is a full MANUAL entry.

[23] M. J. Pivovaroff, W. B. Barber, F. E. Christensen, W. W. Craig, T. Decker, M. Epstein, T. Funk, C. J. Hailey, B. H. Hasegawa, R. Hill, J. G. Jernigan, C. Taylor, and K. P. Ziock. Small-animal radionuclide imaging with focusing gamma-ray optics. In F. P. Doty, H. B. Barber, and H. Roehrig, editors, *Penetrating Radiation Systems and Applications V*, volume 5199 of *Proceedings of the SPIE*, pages 147–161, January 2004.

[24] Michael J. Pivovaroff, Klaus P. Ziock, Monica Perea-Fernandez, Mark J. Harrison, and Regina Soufli. Gamma-ray mirrors for direct measurement of spent nuclear fuel. *Nuclear Instruments and Methods in Physics Research A*, 743:109–113, 2014.

[25] Robert Redus. *Charge Trapping in XR-100T-CdTe Cadmium Telluride Detectors Application Note (ANCZT-2 REV. 3).* Amptek, Inc., Bedford, MA, November 2007.

[26] Robert Redus. *Efficiency of XR-100T-CdTe Detectors Application Note (AN-CdTe-001 Rev. 1).* Amptek, Inc., Bedford, MA, May 2010.

[27] S. Romaine, R. Bruni, B. Choi, C. Jensen, K. Kilaru, B. Ramsey, and S. Sampath. Development of light weight replicated x-ray optics, II. In *Society of Photo-Optical Instrumentation Engineers (SPIE) Conference Series*, volume 9144 of *Society of Photo-Optical Instrumentation Engineers (SPIE) Conference Series*, page 1, July 2014.

[28] D. G. Stearns. The scattering of x rays from nonideal multilayer structures. *Journal of Applied Physics*, 65(2):491–506, 1989.

[29] A.C. Thompson, Vaughan, D., and Center for X-ray optics and advanced light source. *X-ray Data Booklet.* Lawrence Berkeley National Laboratory, 2009.

[30] M. C. Weisskopf, H. D. Tananbaum, L. P. Van Speybroeck, and S. L. O'Dell. Chandra X-ray Observatory (CXO): overview. In J. E. Truemper and B. Aschenbach, editors, *X-Ray Optics, Instruments, and Missions III*, volume 4012 of *Society of Photo-Optical Instrumentation Engineers (SPIE) Conference Series*, pages 2–16, July 2000.

[31] D. L. Windt. IMD: Software for modeling the optical properties of multilayer films. *Computers in Physics*, 12:360–370, 1998.

[32] H. Wolter. Optical image-forming mirror system providing for grazing incidence of rays, August 14 1956. US Patent 2,759,106.

[33] Hans Wolter. Mirror systems with grazing incidence as image-forming optics for x-rays. *Ann. Phys., (Leipzig), ser. 6*, 10:94–114, 1952.